AGU PUBLICATIONS

JGR

Journal of Geophysical Research: Space Physics

RESEARCH ARTICLE
10.1002/2017JA024535

Special Section:
Magnetospheric Multiscale (MMS) Mission Results Throughout the First Primary Mission Phase

Key Points:
- Magnetic reconnection is observed in the magnetosheath
- Reconnection is observed in turbulent environment
- Fluid and kinetic signatures of magnetic reconnection are observed for the first time in the magnetosheath

Correspondence to:
Z. Vörös,
zoltan.voeroes@oeaw.ac.at

Citation:
Vörös, Z., Yordanova, E., Varsani, A., Genestreti, K. J., Khotyaintsev, Y. V., Li, W., … Saito, Y. (2017). MMS observation of magnetic reconnection in the turbulent magnetosheath. *Journal of Geophysical Research: Space Physics*, *122*, 11,442–11,467. https://doi.org/10.1002/2017JA024535

Received 30 JUN 2017
Accepted 25 OCT 2017
Accepted article online 30 OCT 2017
Published online 26 NOV 2017

©2017. The Authors.
This is an open access article under the terms of the Creative Commons Attribution License, which permits use, distribution and reproduction in any medium, provided the original work is properly cited.

MMS Observation of Magnetic Reconnection in the Turbulent Magnetosheath

Z. Vörös[1,2,3], E. Yordanova[4], A. Varsani[2,5], K. J. Genestreti[2], Yu. V. Khotyaintsev[4], W. Li[4], D. B. Graham[4], C. Norgren[4], R. Nakamura[2], Y. Narita[2], F. Plaschke[1,2], W. Magnes[2], W. Baumjohann[2], D. Fischer[2], A. Vaivads[4], E. Eriksson[4,6], P.-A. Lindqvist[7], G. Marklund[7], R. E. Ergun[8], M. Leitner[1], M. P. Leubner[9], R. J. Strangeway[10], O. Le Contel[11], C. Pollock[12], B. J. Giles[12], R. B. Torbert[13], J. L. Burch[13], L. A. Avanov[12], J. C. Dorelli[12], D. J. Gershman[12,14], W. R. Paterson[12], B. Lavraud[15], and Y. Saito[16]

[1]Institute of Physics, University of Graz, Graz, Austria, [2]Space Research Institute, Austrian Academy of Sciences, Graz, Austria, [3]Geodetic and Geophysical Institute, RCAES, Hungarian Academy of Sciences, Sopron, Hungary, [4]Swedish Institute of Space Physics, Uppsala, Sweden, [5]Mullard Space Science Laboratory/UCL, Dorking, UK, [6]Department of Physics and Astronomy, Uppsala University, Uppsala, Sweden, [7]Space and Plasma Group, Royal Institute of Technology, Stockholm, Sweden, [8]Laboratory of Atmospheric and Space Physics, University of Colorado Boulder, Boulder, CO, USA, [9]Institute for Astro- and Particle Physics, University of Innsbruck, Innsbruck, Austria, [10]Institute of Geophysics and Planetary Physics, University of California, Los Angeles, CA, USA, [11]Laboratoire de Physique des Plasmas, CNRS/Ecole Polytechnique/UPMC/Univ. Paris Sud/Obs. de Paris, Paris, France, [12]NASA Goddard Space Flight Center, Greenbelt, MD, USA, [13]Southwest Research Institute, San Antonio, TX, USA, [14]Astronomy Department, University of Maryland, College Park, MD, USA, [15]IRAP, Université de Toulouse, CNRS,CNES, UPS, Toulouse, France, [16]JAXA, Japan

Abstract In this paper we use the full armament of the MMS (Magnetospheric Multiscale) spacecraft to study magnetic reconnection in the turbulent magnetosheath downstream of a quasi-parallel bow shock. Contrarily to the magnetopause and magnetotail cases, only a few observations of reconnection in the magnetosheath have been reported. The case study in this paper presents, for the first time, both fluid-scale and kinetic-scale signatures of an ongoing reconnection in the turbulent magnetosheath. The spacecraft are crossing the reconnection inflow and outflow regions and the ion diffusion region (IDR). Inside the reconnection outflows D shape ion distributions are observed. Inside the IDR mixing of ion populations, crescent-like velocity distributions and ion accelerations are observed. One of the spacecraft skims the outer region of the electron diffusion region, where parallel electric fields, energy dissipation/conversion, electron pressure tensor agyrotropy, electron temperature anisotropy, and electron accelerations are observed. Some of the difficulties of the observations of magnetic reconnection in turbulent plasma are also outlined.

1. Introduction

Magnetic reconnection is almost routinely observed at large-scale boundaries such as the Earth's magnetopause (e.g., Burch et al., 2016; Paschmann et al., 1979; Phan et al., 2004; Russell & Elphic, 1979) and the magnetotail current sheet (e.g., Nagai et al., 2015; Nakamura et al., 2006; Øieroset et al., 2001; Runov et al., 2003). Yet the details of reconnection physics, specifically over kinetic scales, are largely unknown. The large-scale reorganizations of the magnetic field leading to the initiation or suppression of reconnection in different plasma environment is also an unclear issue and needs to be further studied. Perhaps our limited knowledge explains why the occurrence of magnetic reconnection in the solar wind was discovered relatively later (Gosling, 2012; Gosling et al., 2005). It was speculated that reconnecting current sheets might occur at compressed leading edges of interplanetary coronal mass ejections (McComas et al., 1994), which can lead to a significant erosion of magnetic flux in the clouds (Lavraud et al., 2014). Recently, it was also found that the erosion via reconnection can occur at both leading and trailing edges of magnetic clouds (Ruffenach et al., 2015). Another generation mechanism of reconnecting thin current sheets might be turbulence and the associated nonlinear processes in the solar wind (Matthaeus & Lamkin, 1986).

In this paper we study magnetic reconnection in the terrestrial magnetosheath. Reconnecting current sheets can be locally generated or convected to the magnetosheath from the solar wind. Both the solar wind

and the magnetosheath are plasma environments where the plasma β can vary a lot, reaching values $\beta \geq 1$. In general, reconnection can be suppressed if the difference of plasma β across the current sheet is large and the magnetic shear angle Θ_{SH} is small (Phan et al., 2010). The shear angle is defined as an angle between magnetic field vectors $\boldsymbol{B}_i$ and $\boldsymbol{B}_j$, where the (i and j) pairs are taken at the opposite sides of the current sheet. Θ_{SH} has formally the same definition as the magnetic rotation angle θ_{ij} (equation (1) below), where the (i and j) pairs are taken between two spacecraft or between two arbitrary time instants. In plasmas with large fluctuations of plasma β across the current sheet and $\Theta_{SH} < 100°$ the occurrence frequency of magnetic reconnection can be significantly reduced (Phan et al., 2010).

To our knowledge, there were only three detailed magnetosheath reconnection event studies published so far (Phan, Paschmann, et al., 2007; Retinò et al., 2007; Yordanova et al., 2016). This might indicate that reconnection is suppressed in the magnetosheath or the possible events were overlooked, as it happened also in the solar wind before (Gosling, 2012). In any case, based on Magnetospheric Multiscale (MMS) observations, here we provide an event study, which can elucidate some important aspects of the observation of fluid- and kinetic-scale signatures of ongoing magnetic reconnection in the terrestrial magnetosheath. Before introducing the existing results on magnetic reconnection from previous studies, we shortly describe the turbulent plasma environment downstream of a quasi-parallel (QPar) shock, where we searched for possible reconnection events.

Plasma turbulence is stronger downstream of a QPar shock, when the shock normal (N) and the direction of the interplanetary magnetic field (B) are nearly aligned ($0° \leq \theta_{BN} \leq 45°$). It is well known that a QPar shock reflects ions upstream which strongly interact with the impinging solar wind forming the foreshock region. From single spacecraft missions and mainly from Cluster mission it became clear that these interactions at the shock and the back-convected foreshock fluctuations result in different instabilities generating large-amplitude nonlinear structures, such as shocklets, cavitons, or large-amplitude magnetic structures (Burgess et al., 2005; Scholer et al., 2005). In this respect, solar wind transients and discontinuities hitting the bow shock are important drivers of complex interactions in this region as well (Savin et al., 2012; Sibeck et al., 2000). As a result, the QPar shock surface is strongly rippled and the local curvature variations can generate fast jets penetrating to the magnetosheath (Hietala et al., 2009). Indeed, a statistical study based on 4 years of THEMIS (Time History of Events and Macroscale Interactions during Substorms) mission observations of the magnetosheath close to the shock have shown that the vast majority of high dynamic pressure fast jets are associated with the local ripples of a QPar shock (Hietala & Plaschke, 2013). The same THEMIS data were used to show that the potentially geoeffective jets of cross-sectional diameter larger than 2 R_E, depending on the cone angle θ_{BN}, impact the magnetopause 3–9 times per hour. It is estimated that these large jets carry a significant amount of energy, mass, and momentum to the magnetopause, where they can locally trigger surface waves, reconnection, and other geoeffective processes (Plaschke et al., 2016).

The rippled-structured QPar shock and the fast jets are also suggested by recent global hybrid and fully kinetic simulations of the terrestrial magnetosheath (Karimabadi et al., 2014). Although the simulations show more elongated than the more flattened jets observed by THEMIS in propagation direction, there is a qualitative agreement that the penetrating jets are dynamically important in the magnetosheath. The simulations also show that fast jets can stir the whole volume of the magnetosheath, generating vortices, turbulence, wavefronts, magnetic islands (flux ropes), and reconnecting current sheets (Karimabadi et al., 2014). This indicates that multiscale interactions and structure formation are not occurring at the shock or magnetopause only, but there might be a significant dynamical evolution and turbulence generation (Huang et al., 2017; Yordanova et al., 2008) in the wider volume of the magnetosheath as well. This opens the possibility that plasma turbulence might play a role in local generation or evolution of structures in the magnetosheath. An early analytical study of both ideal and resistive instabilities has indicated that MHD turbulence can spontaneously develop into flat or elongated current structures (Carbone et al., 1990). High Reynolds number 2-D MHD simulations also suggested that plasma turbulence may develop into discontinuities, which are identified as ion-scale current density structures. For the quantitative description of the "strength" of discontinuities the normalized changes in the magnetic field vector, the magnetic field increments are widely used, both in simulations and data analysis (Greco et al., 2008). In 2-D MHD simulations, the strongest discontinuities are reconnecting current sheets (Servidio et al., 2011). Recent fully kinetic 3-D simulations of collisionless plasma turbulence also suggested the development to the current structures as well, indicating that the kinetic-scale sheet-like structures are places of increased heating and dissipation (Wan et al., 2015). In terms of the frequency of occurrence and strength, discontinuities in the turbulent solar wind exhibit very similar statistical features

as current sheets in turbulence simulations (Greco et al., 2008, 2009, Osman, Wan, et al., 2011). Namely, the strongest discontinuities form the tail of a non-Gaussian probability distribution of currents. The same statistical resemblance has been found between the distributions of strongest discontinuities in the magnetosheath and of strongest currents in simulations (Chasapis et al., 2015; Vörös et al., 2016). There is evidence that ion and electron heating occurs at strong current sheets in the solar wind (Osman, Matthaeus, et al., 2011) and in the magnetosheath as well (Chasapis et al., 2015, 2017; Sundqvist et al., 2007). According to preliminary results based on Cluster data current sheets are abundant in the QPar magnetosheath and therefore might play an important role in plasma heating (Sundqvist et al., 2007; Vörös et al., 2016). A fraction of these currents can be associated with reconnection. However, this conjecture has to be supported by both event studies and a wider statistical analysis for a broad range of upstream solar wind conditions. Below we introduce the results of existing reconnection event studies in the magnetosheath.

Retinò et al. (2007) searched for reconnection in the highly turbulent magnetosheath downstream of a QPar bow shock. Retinò et al. (2007) identified a magnetosheath reconnection event from Cluster data by plotting the relevant physical quantities in the **LMN** coordinate system. Here **L** corresponds to the direction of the maximum variance of the magnetic field, having $\pm B_L$ as the antiparallel reconnecting field. **N** is the current sheet normal and $\mathbf{M} = \mathbf{N} \times \mathbf{L}$ is the out-of-plane direction. The time duration of the current sheet crossing was very short, ~0.5 s, which corresponded to current sheet thickness of $1\lambda_i = 100$ km. Reconnection was identified on the basis of typical signatures, such as the tangential electric field E_M, nonzero normal magnetic field B_N, plasma inflow V_N and outflow V_L, Hall magnetic field B_M, Hall electric field E_N, and electromagnetic energy conversion term $E.J > 0$. Since the current sheet crossing was short, the plasma speeds were estimated from $\mathbf{E} \times \mathbf{B}/\mathbf{B^2}$, keeping in mind that Cluster measured only the spin plane electric field. Also, the 4 s resolution plasma moments from Cluster did not allow to study electron/proton demagnetization directly. In the Retinò et al. (2007) event, the four Cluster spacecraft observed similar profiles of the magnetic field indicating that the ion-scale current sheet was planar or time stationary.

Phan, Paschmann, et al. (2007) observed another magnetosheath reconnection event by Cluster, an exhaust crossing with a duration of 15 s (10 ion skin depths). Additionally to the reconnection signatures in Retinò et al. (2007) paper, Phan, Paschmann, et al. (2007) identified the rotational discontinuities at the reconnection exhausts boundaries and counter-streaming ion beams indicating magnetic connection across the outflow region. However, the outflow speed V_L was identified on the basis of four measured values only and the perpendicular to magnetic field component $V_{L\perp}$ representing a real outflow speed was not estimated. Moreover, not all four Cluster spacecraft, separated by a distance of 2 R_E, observed the reconnection signatures. This could be explained by limited spatial extent or time evolution of reconnection (Phan, Paschmann, et al., 2007). In this case upstream observations of the same current sheet were available. The ACE and Wind spacecraft observed a thick current sheet in the solar wind, which presumably was carried to the magnetosheath, where the observed reconnection was initiated due to local compressions (Phan, Paschmann, et al., 2007). In fact, a study using MMS data has shown that fast magnetosheath shear flows can locally generate ion-scale current sheets with nonplanar 3-D structure (Eriksson, Vaivads, et al., 2016).

The first magnetosheath reconnection event using the high-resolution MMS data was published by Yordanova et al. (2016). This event occurred in the compressed turbulent QPar magnetosheath and was associated with a high-density compressional region at the leading edge of a high-speed solar wind stream. MMS observed strong short duration electron-scale currents, electron heating, fast electron jets, narrow electric field structures, and electron pressure anisotropy. The electron inertial length was ~0.7 km, while the distance between the spacecraft was ~10 km. The narrow structures were seen by all spacecraft over a period of less than 2 s. At the same time, the out-of-plane components of the electric field in the generalized Ohm's law were enhanced. Electron and ion particle data indicated that the MMS spacecraft did not enter the electron diffusion region but the spacecraft crossed the ion diffusion region near an X line, where ions were demagnetized and organized to two distinct hot and cold populations. Although the plasma, field, and particle signatures were considered by Yordanova et al. (2016) as imprints of the crossing of the separatrix region of magnetic reconnection in the QPar magnetosheath, this event does not match fully the exhaust boundary structure of the Phan, Paschmann, et al. (2007) event.

In the above case studies it was found that magnetosheath turbulence or/and compressions were important in triggering or generating reconnection at thin current sheets. Obviously, more event studies are needed to confirm these findings. However, previous studies have also shown that compressions can trigger

reconnection in the sheath of interplanetary coronal mass ejections (Feng & Wang, 2013) or in the Earth's magnetotail (Vörös et al., 2014).

Our primary interest in this paper is to identify reconnecting current sheet signatures in the QPar magnetosheath. The first difficulty concerns finding the location of a reconnection site in a turbulent environment. The magnetopause or the tail current sheet as large-scale boundaries is very clearly seen in the data; therefore, we know where to search for a reconnection event. On the other hand, there are numerous current sheets and plasma flows (potential exhausts) in the magnetosheath, which might be associated with a reconnection in any location or time. In order to find reconnection events which are not suppressed in the high β environment, we prefer current sheets with large magnetic shears Θ_{SH}. However, it is difficult to calculate the actual shear angle when the current sheet crossings are not along the normal direction. In such cases the current sheet geometry has to be determined first in the LMN system. In a turbulent 3-D environment the quasi-2-D reconnection geometry and so the LMN coordinate system may not exist. Our strategy here is to determine the LMN coordinate system, possibly by using different methods, and then test the consistency of reconnection observations in the same system. Consistency means that, for example, in the given LMN system, the outflow/inflow directions and locations, the electric and magnetic field and current directions, the locations of the diffusion regions or the approximate position of the X line, and the local kinetic particle signatures show features as expected during a reconnection crossing. The expected reconnection signatures will be gradually explained below. When the reconnection geometry is known, the magnetic shear angle Θ_{SH} can be calculated.

The paper is organized as follows: section 2 explains the data and instrumentation and provides the overview of the selected reconnection event. In section 3 the determination of the reconnection LMN coordinate system is described. In section 4 the magnetic field, ion, and electron velocities are shown in the LMN coordinates. Fluid signatures of magnetic reconnection are tested in section 5. Section 6 contains the identification of key regions and processes including the observations of ion diffusion region (IDR) and electron diffusion region (EDR). Summarizing the findings, section 7 provides a reconnection cartoon in which the basic observables are explained in detail. The kinetic signatures of magnetic reconnection and more insights to convective electron outflows are explained in section 8. Finally, section 9 contains the discussion and conclusions.

2. Data and Instrumentation

It is the unprecedented high time resolution plasma measurements which make the MMS mission unique. Ion and electron moments from Fast Plasma Investigation instrument (Pollock et al., 2016) have time resolution 150 ms and 30 ms, respectively. The electric field data from Electric Double Probes (EDP) instrument are available with time resolution of 8 kHz (Ergun et al., 2016; Lindqvist et al., 2016; Torbert et al., 2016). The merged digital fluxgate (FGM) (Russell et al., 2016) and search coil (SCM) (Le Contel et al., 2016) data were developed by using instrument frequency and timing models that were created during the FIELDS integration test campaign (Torbert et al., 2016). These models are based on linear filter functions and can correct the respective frequency responses of the instruments in gain and phase. Using these models, in-flight data were corrected and data were added using low- and high-pass filter functions. Thus, the data set analyzed here consists of data below 4 Hz originating from FGM, data above—from SCM and in the crossover region both data sets were used (Fischer et al., 2016).

2.1. Event Overview

On 30 November 2015 between 00:21:00 and 00:26:30 UT the MMS spacecraft were located in the compressed turbulent magnetosheath, downstream of a quasi-parallel bow shock. During this time interval high-resolution MMS data are readily available.

Our event overview plot (Figure 1) shows observations from MMS1 in GSE and some parameters derived from pairs of spacecraft with respect to MMS1 in the interval between 00:23:43 and 00:24:13 UT. Figure 1a shows the total magnetic field B_T and the components B_X, B_Y, andB_Z. We will concentrate on the time interval from 00:23:50 to 00:24:04 UT, in the dashed black box, which highlights two enhancements of B_T reaching 70 and 82 nT with maxima at 00:23:51 and 00:23:57 UT, respectively (Figure 1a). In the blue dashed box, roughly from 00:23:52.5 to 00:23:57 UT, B_T is significantly decreased, reaching 8 nT after 00:23:55 UT. Figures 1b and 1c show the ion (*Vi*) and electron (*Ve*) velocity components. The velocity components are predominantly negative or close to zero except for the time interval between 00:23:50 and 00:23:56 UT, when Vi_Z and Ve_Z

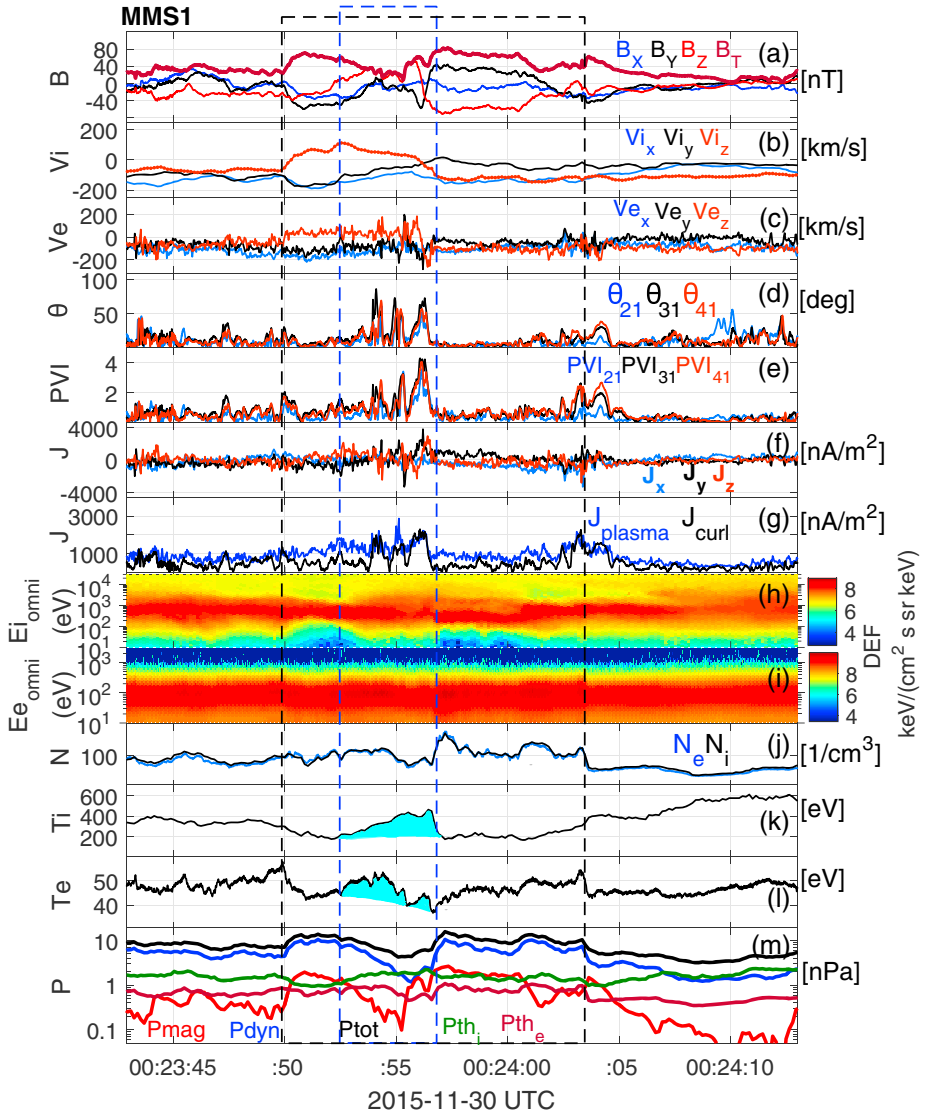

Figure 1. Overview of the event observed by MMS1: (a) magnetic field intensity B_T and components (B_X, B_Y, B_Z); (b, c) ion (Vi_X, Vi_Y, Vi_Z) and electron (Ve_X, Ve_Y, Ve_Z) velocities; (d, e) magnetic field rotation angle θ_{ij} and partial variance of increments PVI_{ij} between the pairs of spacecraft with respect to MMS1 ($i, j = 1, 2, 3, 4$); (f) current calculated from plasma data (J_X, J_Y, J_Z); (g) comparison between the total plasma current J_{plasma} from MMS1 and the curlometer current J_{curl} from spacecraft tetrahedron; (h, e) omnidirectional ion and electron differential energy flux spectrograms; (i) ion N_i and electron N_e density; (k, l) ion T_i and electron T_e temperature; (m) total Ptot, magnetic Pmag, dynamic Pdyn, ion Pth_i and electron Pth_e thermal pressures. The black dash box confines the interval of enhanced total pressure. The blue box highlights the region of enhanced currents within which the ion and electron temperature is also locally enhanced (filled-in areas in cyan in Figures 1k and 1l). All vector quantities are in GSE coordinate system.

components reverse direction and are predominantly positive. Relative to the background magnetosheath flows the *Vi* and *Ve* velocities are also enhanced in −X and −Y directions at the beginning of the same time interval. The correlated changes of *B* and *Vi* components at the leading (after 00:23:50 UT) and trailing (before 00:23:56 UT) edges of the enhanced plasma velocity interval indicate that the spacecraft might cross here a reconnection exhaust, including its boundaries. This would make the event similar to the previous observations of single reconnection exhausts in the magnetosheath by Retinò et al. (2007) and Phan, Paschmann, et al. (2007). However, as will be shown later, our event represents a more complicated crossing of a reconnection region, including a flow reversal and signatures of ion and electron diffusion regions (IDR and EDR), respectively.

The first two derived quantities are the magnetic rotation angle θ_{ij} and the so called partial variance of increments PVI_{ij}, calculated between spacecraft pairs (or two time instants) i, j. The magnetic rotation angles are defined as

$$\theta_{ij}(t) = \cos^{-1} \frac{\boldsymbol{B}_i(t) \cdot \boldsymbol{B}_j(t)}{|\,\boldsymbol{B}_i(t)\,| \cdot |\,\boldsymbol{B}_j(t)\,|}. \quad (1)$$

The PVIs are obtained as

$$PVI_{ij}(t) = \sqrt{\frac{|\,\Delta\boldsymbol{B}_{ij}(t)\,|^2}{\langle |\,\Delta\boldsymbol{B}_{ij}\,|^2 \rangle}}, \quad (2)$$

where t is time and the averaging $\langle\rangle$ is over the whole time interval. PVI is extensively used in studies of turbulence to detect discontinuities (e.g., Greco et al., 2008, 2009). In the first step we used these parameters and the decreasing strength of the magnetic field, to locate the potentially reconnecting current sheets in time series. We repeat that such a preliminary location of the event in time is not needed at large-scale boundaries. Figures 1d and 1e show these quantities for three combinations of spacecraft pairs only. The angles θ associated with the current sheets are relatively small (70–90°) when calculated between spacecraft i, j pairs separated by the ~10 km distance. However, θ becomes larger when the i, j subscripts correspond to time instants at wider spatial separations. For example, when the whole magnetic field rotation is considered for the third discontinuity, for which $PVI_{ij} \sim 4$, θ increases to 170°. This indicates that the thickness of this structure comprising the nearly antiparallel fields is larger than the distance between the spacecraft.

The other derived quantities are the current densities. The components of $\mathbf{J_{plasma}} \equiv (J_x, J_y, J_z)$, obtained from $Nq(\mathbf{V_i} - \mathbf{V_e})$ (N - plasma density, and q - charge of particles), are shown in Figure 1f. In Figure 1g the magnitude of $J_{plasma} = |\,\mathbf{J_{plasma}}\,|$ is compared to the magnitude of current density $J_{curl} = |\,\mathbf{J_{curl}}\,|$, obtained from the tetrahedron curlometer technique (Dunlop et al., 2002). As seen in Figure 1g, $J_{plasma} \sim J_{curl}$, mainly when the currents are small or when their duration in time is short. After resampling and smoothing the current time series the ratio J_{plasma}/J_{curl} was calculated. For example, for the narrow current structures between 00:23:54 and 00:23:56 UT or between 00:24:03 and 00:24:05 UT the ratio J_{plasma}/J_{curl} is close to 1 (not shown). However, locally $J_{plasma}/J_{curl} > 1$ also occurs, for example, between 00:23:50 and 00:23:53 UT. For this time interval, $J_{plasma}/J_{curl} \sim 2.5$ for each MMS spacecraft (not shown). This might indicate that there is a systematic error in the calculation of the current density or that the separation distance between the spacecraft, a key scale limitation in the curlometer technique, does not match the spatial scales of the local currents. Actually, Figure 1a shows that between 00:23:50 and 00:23:53 UT (with $J_{plasma}/J_{curl} \sim 2.5$) there is a slow rotation in the magnetic field, while the magnetic rotations at the peak values of currents are much faster.

The omnidirectional ion and electron fluxes are shown in Figures 1h and 1i. The ion fluxes exhibit local broadenings and narrowings of the distribution over the displayed energy range. There exist ions reaching 30 keV associated with the enhanced currents and structures inside the blue dashed box. By contrast, the high energy ion population seen after 00:24:07 UT is not associated with locally enhanced currents or PVIs, also showing dispersion features with the most energetic ions appearing first. These features might indicate that the energetic ions associated with the currents are locally generated, while the source region of the dispersed ions is remote. The omnidirectional electron fluxes exhibit intermittent enhancements around 100 eV.

Plasma densities (N_e, N_i), ion (T_i) and electron (T_e) temperatures are depicted in Figures 1j–1l. The blue filled areas in Figures 1k and 1l visualize the time intervals when the ion and electron temperatures associated with current structures are locally enhanced. Finally, the total (Ptot), dynamical (Pdyn), magnetic (Pmag) and ion (Pth_i) and electron (Pth_e) thermal pressures are shown in Figure 1m. The total pressure is not constant during the whole time interval, suggesting that the underlying structures are not fully pressure balanced. Although the total pressure is mainly determined by the dynamic pressure, there also exist local anticorrelations between B_T and N, T_i, T_e (Figures 1a and 1j–1l) or between the different pressure terms (e.g., from 00:24:00 to 00:24:025 in Figure 1m), which can occur due to the diamagnetic effect.

3. LMN Coordinate System Determination

We suppose that for our event, there exists an LMN coordinate system in which the reconnection physics can be properly studied. While this assumption usually works well for many reconnection events observed at large-scale boundaries (magnetopause and magnetotail), it is not obvious that the same is valid in the

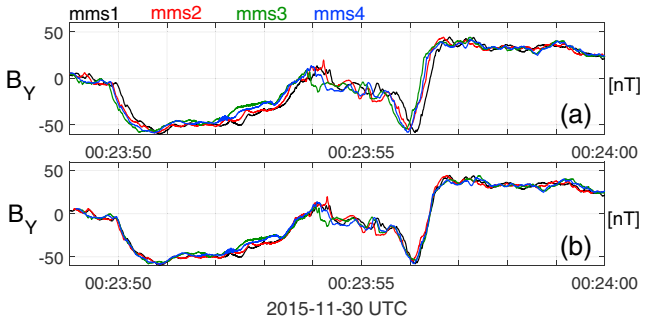

Figure 2. Application of the multispacecraft timing (MST) on a structure in B_Y magnetic field component after 00:23:56 UT. (a) B_Y measurements for all spacecraft; (b) B_Y after the timing procedure (see section 3 for details). The time shift is approximately the same at different times.

turbulent magnetosheath. In determining the LMN system first we try the minimum variance analysis (MVA) of **B** between 00:23:51 and 00:23:56 UT, which is the wider time interval with enhanced $\mathbf{J_{plasma}}$ and decreased B_T (Figures 1a and 1g). The quality of the MVA results is usually quantified in terms of the robustness of the large enough ratios of eigenvalues $r_{12} \equiv \lambda_1/\lambda_2$ and $r_{23} \equiv \lambda_2/\lambda_3$ associated with eigenvectors in maximum (**L** : λ_1) intermediate (**M** : λ_2) and minimum (**N** : λ_3) variance directions of the field components, respectively. For the considered time interval we obtained $r_{12} \sim 6$ and $r_{23} \sim 4$. Similar ratios are obtained for all MMS spacecraft. These small eigenvalue ratios already indicate that the MVA over the considered time interval does not provide the correct LMN system. There are no generally accepted thresholds for r_{ij}s. Knetter et al. (2004) compared different methods for the determination of discontinuity normal directions, and they found that the MVA normals are satisfactory when $r_{23} \geq 8$. Also, for the above considered interval, the r_{ij}s change substantially when the length of the data interval is slightly changed. A more robust MVA estimate is obtained for the time interval between 00:23:55.97 and 00:23:56.39 UT (MMS1 spacecraft), which corresponds to the largest rotation of the magnetic field at the right end of the blue dashed box in Figure 1a. For this interval $r_{12} \sim 15$ and $r_{23} \sim 13$. Similar ratios are obtained for the other spacecraft by shifting the time intervals to the position of the local largest magnetic rotation or current sheet. The obtained average eigenvectors are **L** = [−0.07 −0.55 0.83], **M** = [0.15 0.82 0.55], and **N** = [−0.99 0.17 0.03] GSE.

Since several current and field structures are observed by each MMS spacecraft during the considered event, the relative positions and times of the occurrence of structures are used for multispacecraft timing (MST) as well (Sonnerup et al., 2008). We applied MST on magnetic field structures at the largest rotation of the magnetic field and obtained the following estimate for the normal direction **N** = [−0.97 ± 0.03 0.22 ± 0.08 −0.05 ± 0.11] GSE. It can be seen that the MST normal eigenvector agrees well with the MVA normal within error bars. Figure 2 demonstrates how MST works on the B_Y components of the magnetic field. The MST normal is calculated at several time instants during the large rotation of magnetic field after 00:23:56 UT (Figure 2a), and the obtained time delays of structures between the spacecraft are used to shift the B_Y time series to new time positions. Figure 2b shows that the time shift collapses the data from different spacecraft nearly to one curve not only at 00:23:56 UT but also after 00:23:50 and 00:23:53 UT. This indicates that the estimated normal direction determined for the relatively small separation of spacecraft is valid over a longer time interval ~6 s. The normal velocity of the underlying structure from the MST analysis is V_N(MST) = [−103 ± 6 25 ± 10 −10 ± 5] km/s GSE. The distance between the most separated spacecraft (MMS3-1) along *N* is ~22 km which corresponds to a time shift ~0.2 s.

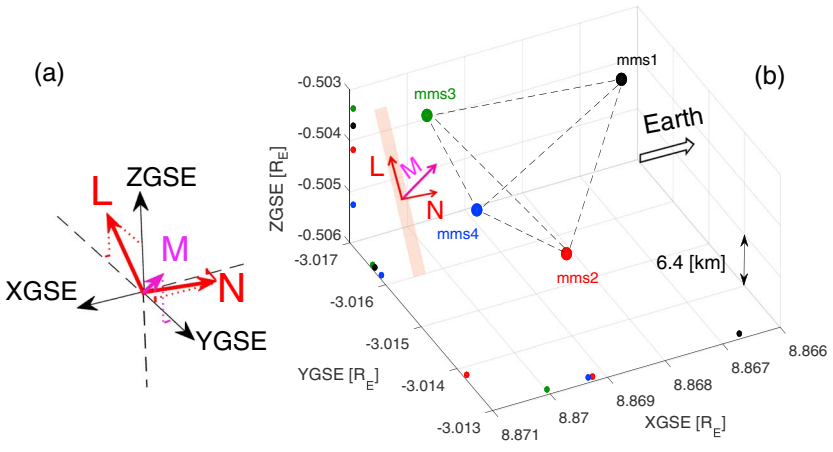

Figure 3. Positions and coordinate systems: (a) relative orientation of the GSE and LMN axes; (b) 3-D spacecraft tetrahedron position in GSE with the structure (light brown stripe) and its orientation in LMN.

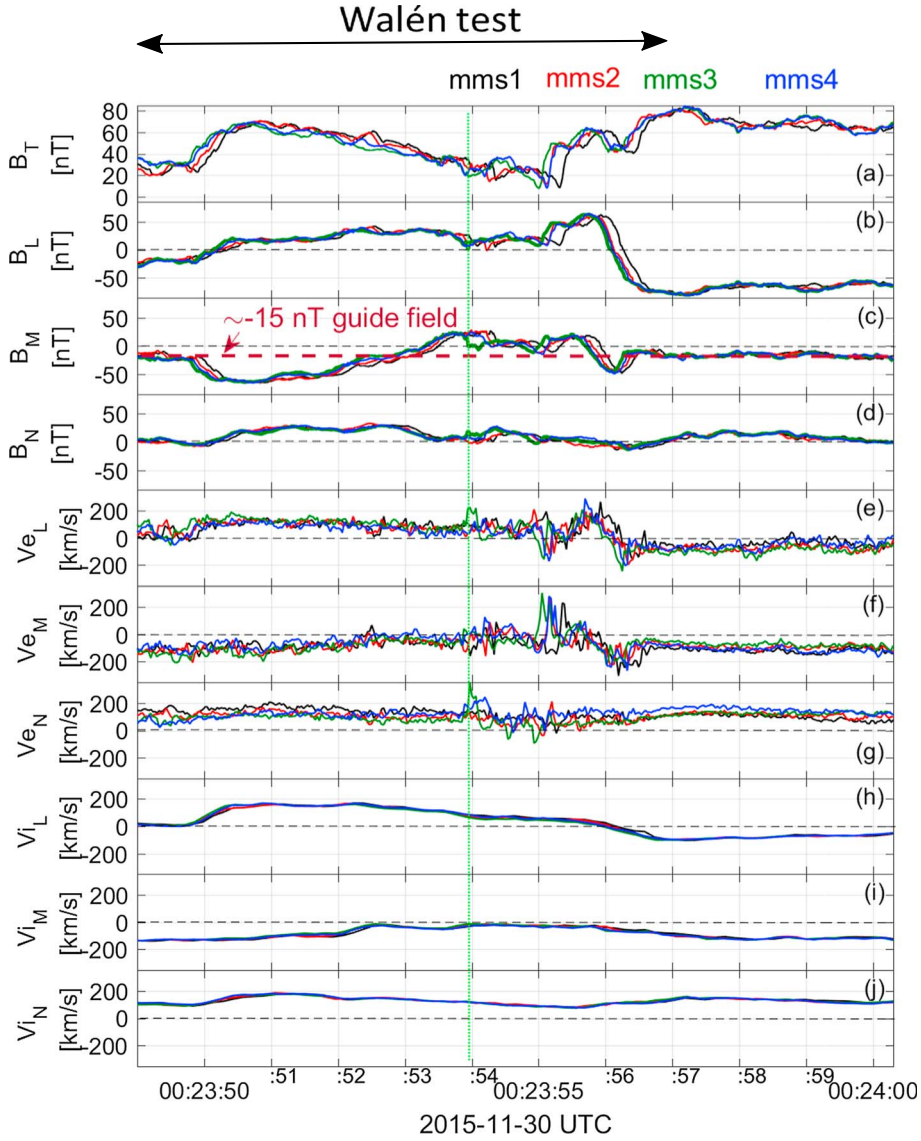

Figure 4. The event in LMN frame: (a–d) total magnetic field and magnetic field components (e–g) electron velocity components; and (h–j) ion velocity components, respectively. The green dotted vertical line marks the location of MMS3 being the closest spacecraft to the current sheet. The dark red dash line in Figure 4c shows the level of the guide field. The black double arrow on top of the figure marks the interval over which the Walén test was performed.

In what follows the averaged MVA LMN eigenvectors will be used. Figure 3a shows the LMN directions in the GSE coordinate system while the positions of MMS spacecraft are depicted in Figure 3b. The projected positions of the spacecraft are indicated on XYZ GSE axes by color-coded balls. The figure also shows that a structure with a −XGSE normal direction moving toward the Earth crosses the MMS3-4-2 spacecraft first and after ∼ 0.2 s reaches MMS1. This ordering can be clearly seen in Figure 2a.

4. The Event in the LMN Coordinate System

Figure 4 shows the basic variables rotated to the LMN system for all four MMS spacecraft. Figures 4a–4d show the total magnetic field and its components, Figures 4e–4g the electron velocity (*Ve*), and Figures 4h–4j the ion velocity (*Vi*) components for the MMS spacecraft. The striking feature is the smooth variation of the ion velocity in comparison with the structured narrow bursts in the electron velocity. Similar differential motions between electrons and ions have been observed by MMS spacecraft during a magnetosheath reconnection

event by Yordanova et al. (2016). The possible reconnection outflows seen in GSE *Vi* and *Ve* (Figures 1b and 1c) are preserved in the LMN Vi_L and Ve_L coordinates with a flow reversal near 00:23:56 UT (Figures 4e and 4h). We note that the occurrence of ±L directional electron and ion flows represents a necessary but not sufficient condition for the occurrence of reconnection. For example, the ±L directional flows can be associated with a flow shear or L directional parallel to **B** stream of particles and not a real perpendicular to **B** plasma convection. Evidently, further investigations are needed to confirm the occurrence of magnetic reconnection. We will return to this question in section 6.1.

The dotted vertical green line at ~00:23:53.95 UT in Figure 4 shows the time instant when the MMS3 spacecraft observes $B_L \sim 3$ nT, $B_M \sim 0$ nT, and $B_N \sim 19$ nT. The neighborhood of this time instant is shown in more detail on top of Figure 7. At other MMS spacecraft the B_N components do not dominate; therefore, MMS3 reaches the closest position relative to the current sheet. Also, the narrowly peaked fluctuations seen in $\mathbf{V_e}$ components start at the dotted green line lasting until 00:23:56.6 UT (Figures 4e–4g), which is the end time of the large magnetic field rotation (Figures 4b and 4c). As it will be shown later, during this time interval the spacecraft cross the EDR, IDR, and electron jet regions of magnetic reconnection.

Figure 4c shows that there exist a $B_g \sim -15$ nT guide field, while the maxima of B_{Lmax} in Figure 4b reach +65 and −75 nT. This results in $B_g \sim 0.2(|B_{\mathrm{Lmax}}|)$.

5. Fluid Signatures of Magnetic Reconnection

At large-scale boundaries, for example, the magnetopause, the occurrence of reconnection, and the associated Alfvénic outflows come from the assumption that the transport of plasma through the boundary takes place across a rotational discontinuity (RD) with nonzero normal magnetic field B_N, indicating the presence of magnetically connected regions. In this picture, the outflows generated by magnetic reconnection should match the local Alfvén velocity in the moving frame of reconnection structure in which the electric field vanishes. According to the Faraday's law an approximately zero electric field corresponds to a quasi-static magnetic structure. This coordinate system is called the de deHoffmann-Teller (HT) frame and the static magnetic structure is moving with the velocity $\mathbf{V_{HT}}$. The so-called Walén test is used to check if correlations exist between the Alfvén velocity $\pm\mathbf{V_A}$ and $\mathbf{V} - \mathbf{V_{HT}}$, where **V** is the plasma velocity and the ± signs correspond to outflows in ±L directions, matching also the ± sign of the normal magnetic field B_N. Accordingly, in the scatterplot of the Alfvén velocity versus plasma velocity in HT frame a correlation with linear regression slope near ±1 should be observed within the reconnection outflows (Paschmann et al., 2005; Paschmann & Sonnerup, 2008; Sonnerup et al., 1987).

The implications of the Walén test comparing MHD-scale velocities might not be straightforward for the turbulent magnetosheath. The ion inertial range, d_i is roughly 20 km and a structure of this size moving with $V_N \sim 100$ km/s is seen 0.2 s. The duration of the magnetic field rotation near 00:23:50 UT is about 0.8 s (Figure 4). This means that the spacecraft are close to the reconnection site. Nevertheless, a simple test comparing the change of the plasma velocity $\Delta\mathbf{V}$ with the corrected change of the Alfvén velocity $\Delta\mathbf{V}(\mathrm{predicted}) = \pm\sqrt{\xi}\Delta\mathbf{B}/\sqrt{(\mu_0 N)}$ indicates a possible RD-like structure (Chao et al., 2014; Phan et al., 2004). Here $\xi = 1 - \mu_0(P_{||} - P_{\perp})/B^2$ is the pressure anisotropy factor, μ_0 is the permeability of the vacuum, and $P_{||}$ and $P_{\perp}$ are the thermal pressures parallel and perpendicular to local **B**. For example, for MMS1 ΔB_L across the discontinuity is 39 nT (changing from −19 to +20 nT), the average anisotropy factor is $\xi = 1.5$ (not shown), $N \sim 100$ p/cm^3 (Figure 1j) gives $\Delta V_L(\mathrm{predicted}) \sim 104$ km/s, while $\Delta V_L \sim 110$ km/s (changing from 40 to 150 km/s) in Figure 4h. Here we observe that at MMS1 the magnetic field rotation starts at 00:23:50 and ends at 00:23:50.8 UT. Similar calculations give $\Delta V_N(\mathrm{predicted}) \sim 69$ km/s and $\Delta V_N \sim 70$ km/s. Although, there is a significant change in the B_M component from −19 to −61 nT (Figure 4c), which leads to $\Delta V_M(\mathrm{predicted}) \sim 112$ km/s, $\Delta V_M \sim 0$ km/s. This can be explained by the fact that the rotational structure is rather thin and in the M direction, supposing that we are dealing with magnetic reconnection, a significant Hall field is present below the −15 nT guide field (Figure 4c). On the other hand, the large-amplitude rotation of the magnetic field near 00:23:56 UT cannot explain the small changes in *Vi*. For example, ΔB_L across this discontinuity is 135 nT (changing from +60 to −75 nT) which would correspond to $\Delta V_L(\mathrm{predicted}) \sim 360$ km/s; however, $V_L \sim 150$ km/s is observed (Figures 4b and 4h). Therefore, the observed structure cannot be consistent with a RD. The comparison of GSE **B** and $\mathbf{V_i}$ components leads to the same results. In order to demonstrate further that the pressure anisotropy is not associated with instabilities which would significantly affect $\Delta\mathbf{V}(\mathrm{predicted})$ at the discontinuities the time series of B_L and Vi_L (Figures 5a and 5b) are plotted together with the ratio

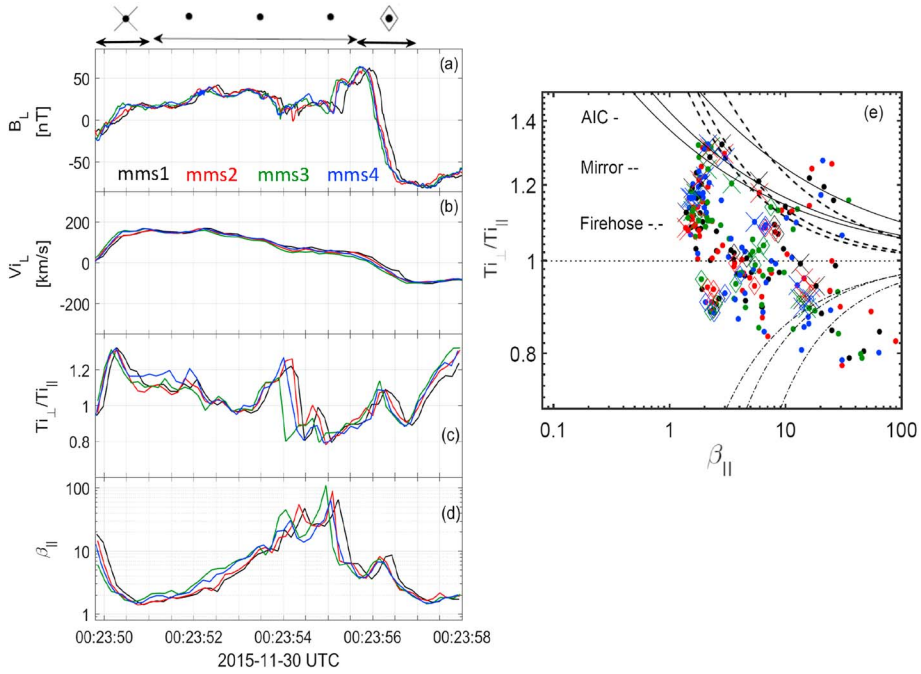

Figure 5. Temperature anisotropy constraints. (a) B_L. (b) Vi_L. (c) The ratio of perpendicular to parallel ion temperatures $Ti_\perp/Ti_{||}$. (d) Parallel plasma $\beta_{||}$. (e) The scatterplot of $\beta_{||}$ versus $Ti_\perp/Ti_{||}$ with the overlayed theoretical thresholds of temperature anisotropy instabilities: the continuous lines correspond to Alfvén ion cyclotron (AIC), the dashed lines to mirror and the dashed-dotted lines to fire-hose instability thresholds for different growth rates between 0.1 and 0.0001. The crosses, dots, and diamonds correspond to the time intervals indicated on top of Figure 5a.

of perpendicular to parallel ion temperatures ($Ti_\perp/Ti_{||}$, Figure 5c) and parallel plasma beta ($\beta_{||}$, Figure 5d). The scatterplot of these quantities with the overlayed theoretical thresholds of temperature anisotropy instabilities is shown in Figure 5d. Here the continuous lines correspond to Alfvén ion cyclotron (AIC), the dashed lines to mirror, and the dashed-dotted lines to fire-hose instability thresholds for different growth rates between 0.1 and 0.0001 (Gary et al., 1998; Hellinger & Trávníček 2006; Hellinger et al., 2006; Samsonov et al., 2001). The symbols in the scatterplot (Figure 5e), the crosses, dots, and diamonds, correspond to the time intervals indicated on top of Figure 5a. The fluctuations within the time intervals of magnetic field rotations (crosses and diamonds) considered above seem to be constrained by the instability thresholds, which together with the small average value of ξ ensures that $\Delta\mathbf{V}$(predicted)s are estimated correctly. However, temperature anisotropies grow over the instability thresholds (Figures 5c and 5e) between 00:23:53.5 and 00:23:55.5 UT, when B_L values show minima in a high beta plasma, closer to the current sheet (Figures 5a and 5d).

The deHoffmann-Teller frame velocity $\mathbf{V_{HT}}$ is found through minimization of the quantity (Khrabrov & Sonnerup, 1998)

$$\frac{1}{M}\sum_{m=1}^{M} |\left(\mathbf{V}_m^{i,e} - \mathbf{V}_{HT}^{i,e}\right) \times \mathbf{B}_m|^2 \tag{3}$$

for the set of M measurements, considering both ion and electron velocities, separately. For ions $\mathbf{V}^i_{\mathrm{HT}}$ = [−124 − 78 80] km/s GSE and for electrons $\mathbf{V}^e_{\mathrm{HT}}$ = [−80 − 75 61] km/s GSE was obtained. Despite the differences between ion and electron $\mathbf{V}_{\mathrm{HT}}$s there is a qualitative agreement that the underlying quasi-stationary magnetic structure is propagating toward the Earth having also significant velocity components in −Y and +Z GSE directions. The multispacecraft timing velocity is between the X components of $\mathbf{V}^{i,e}_{\mathrm{HT}}$ velocities: $-124 < -|V_N(\mathrm{MST})| \sim -106 < -80$ km/s.

In Figure 6 the $\mathbf{V_A}$ and $\mathbf{V} - \mathbf{V_{HT}}$ scatterplots are presented and the black, blue, and red points correspond to the velocity components for the time interval between 00:23:49 and 00:23:56.9 UT, indicated at the top of Figure 4. Figures 6a and 6b show the cases associated with $\mathbf{V}^i_{\mathrm{HT}}$ and $\mathbf{V}^e_{\mathrm{HT}}$, respectively. The best linear regressions are obtained when the fits are made for the subintervals from 00:23:49 to 00:23:54.8 UT and from 00:23:54.8 to 00:23:56.9 UT. In this way regression curves with positive and negative slopes are obtained

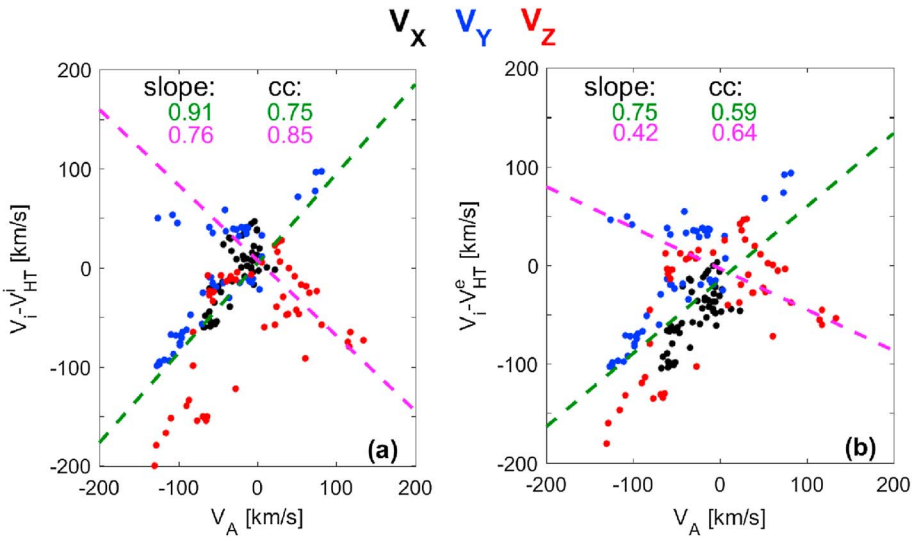

Figure 6. Walén relation test in the deHoffmann-Teller (HT) frame: comparisons between the observed (a) ion and (b) electron velocities in HT frame and the Alfvén velocity. The three velocity components are indicated with color dots. The green and magenta dash lines represent a linear regression fit of the outflows on both sides of the reconnection site together with the respective slopes and correlation coefficients.)

(green and magenta dashed lines), which are associated with predominantly positive and negative B_N components of the magnetic field, respectively (Figure 4d). A more detailed discussion of these intervals comes in the next sessions. The slopes and correlations for these intervals, except for the magenta line in Figure 6b, satisfy the usual conditions required for the Walén test (Zhang, 2016). A change in sign of the slopes can mean either the spacecraft are on the same side of the X line crossing the two boundaries of the same outflow successively or that the other side of the X line is crossed within the same hemisphere of the oppositely directed outflow (Øieroset et al., 2000). Since the changes of the sign of regression slopes are associated with the change of the sign of B_N, we interpret these results as a possible indication that the MMS spacecraft crossed both sides of the reconnection X line. When slightly longer time intervals are considered for the Walén test, the correlations in the scatterplots are lost.

6. More Reconnection Signatures

6.1. Identification of Key Regions

In order to identify more reliably the outflows and the distinct regions of magnetic reconnection the perpendicular to B flows have to be compared to parallel to B flows and to perpendicular convection velocity. Figure 7a shows again the magnetic field, while in Figure 7b the parallel to **B** electron ($Ve_{||L}$) and ion ($Vi_{||L}$) L directional flows are shown. The differential parallel motion of electrons and ions is readily discernible. Figure 7c contains the L directional perpendicular flows, $Ve_{\perp L}$, $Vi_{\perp L}$, and $V_{\perp L} \equiv (\mathbf{E} \times \mathbf{B}/\mathbf{B}^2)_L$. The magnitude of the Alfvén velocity, $\pm V_A$, is indicated by the dashed green line. In Figure 7d the N directional perpendicular ion and electron flows $Ve_{\perp L}$, $Vi_{\perp L}$ are compared to $V_{\perp N} \equiv (\mathbf{E} \times \mathbf{B}/\mathbf{B}^2)_N$.

It can be immediately seen that $V_{\perp L} \sim Ve_{\perp L} \sim Vi_{\perp L}$, except for the time interval between 00:23:53.8 and 00:23:55.2 UT when ions are demagnetized and the spacecraft are crossing the IDR. Between 00:23:54 and 00:23:54.2 UT both ions and electrons seem to be demagnetized. This occurs when $B_M \sim 0$ and B_L is smaller or similar to B_N (zoomed-in magnetic field in the box over the plot). The dotted blue vertical line shows the moment when ion, electron demagnetizations start. Just before, there is a sharp electron outflow reaching $Ve_{\perp L} \sim 160$ km/s. For this short moment ions are still demagnetized. Extended super-Alfvénic electron jets at the outer EDR were predicted by 2-D particle-in-cell (PIC) simulations (Shay et al., 2007) and observed in the magnetosheath (Phan, Drake, et al., 2007) and in the near-Earth magnetotail (Nagai et al., 2011). In our case the electron perpendicular outflow is between $V_{Ap} < Ve_{\perp L} = 160$ km/s $< V_{Ae}$, where $V_{Ap} = 40$ and $V_{Ae} = 1,700$ km/s are the proton and electron Alfvén velocities, respectively. Here $Ve_{\perp L}$ is about an order of magnitude smaller than V_{Ae}. However, it would be premature to conclude that the spacecraft is not near the outer EDR when $Ve_{\perp L}$ is enhanced but smaller than V_{Ae}. First of all, the EDR or its outer region is ambiguously

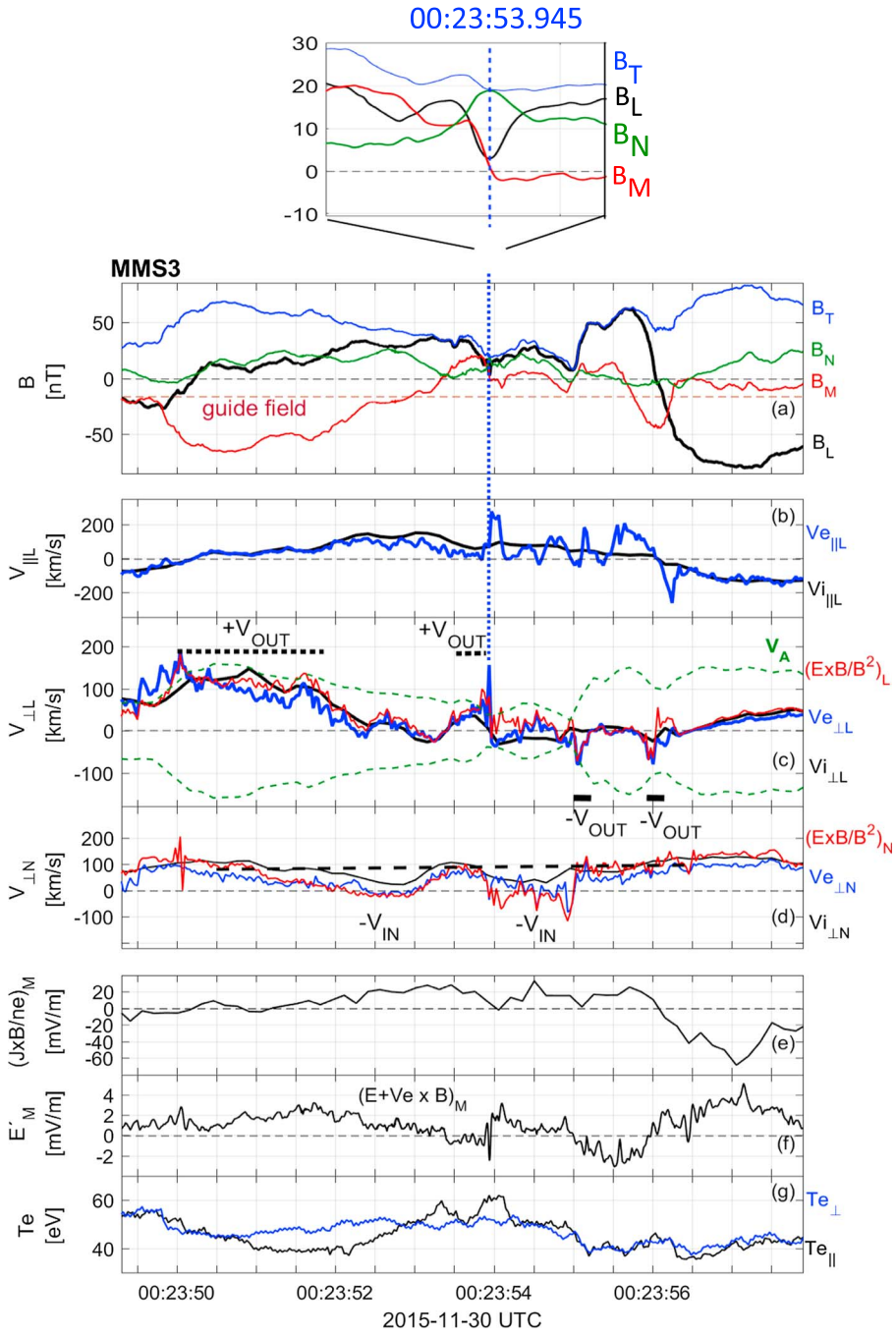

Figure 7. Observation of magnetic reconnection by MMS3 in LMN coordinates. Top panel shows zoom in of the magnetic field components around the vertical dashed blue line. (a) Magnetic field intensity and components. The vertical blue dashed line marks the crossing of the EDR. The dark red horizontal line shows the guide field; (b) parallel to **B** L component of the ion and electron velocity; (c) perpendicular to **B** L component of the ion and electron velocity. The green dash curves stay for ±Alfvén velocity. The red curve is the convection velocity calculated from the fields in L direction. The horizontal black dash bars mark the +L, the solid black bars mark the −L directional perpendicular outflows; (d) perpendicular **B** N components of the ion and electron velocity. The red curve is the N directional convection velocity. The inflow regions are located below the horizontal dash line showing the offset due to the convective motion of the structure toward Earth; (e) M component of the $(J \times B/ne)$ force; (f) M component of the electric field in the electron frame; and (g) parallel and perpendicular to **B** electron temperatures.

defined and the possible signatures also include enhanced energy conversion/dissipation, electron agyrotropy, or characteristic electron velocity distribution functions (VDFs) (Burch et al., 2016; Zenitani & Nagai, 2016). These signatures are considered below. Also, the comparison of data, especially of 3-D reconnection signatures with numerical simulations, is not fully understood. In fact, 2-D PIC simulations have shown that a nonnegligible guide field B_g, for example, equal or larger than 0.05 B_L (our case is 0.2 B_L) can split and deflect the electron jets due to Lorentz force $q\mathbf{V}\times\mathbf{B}_g$ (Goldman et al., 2011). Indeed, the guide field-associated deflection of the electron jets from the neutral sheet was observed in the magnetotail (Zhou et al., 2014). Moreover, different 2-D PIC simulation runs have demonstrated that the structure and the extension of electron current sheets besides the guide field may depend on the ion-to-electron mass ratio, electron beta, and electron pressure anisotropies (Le et al., 2013). The local electron agyrotropy, which is quantifying electron pressure anisotropy, is estimated below.

It is expected that the width of the fast electron jet is roughly 10 km (~9 electron skin depth) (Phan, Drake, et al., 2007). We calculated the perpendicular electron velocities at each spacecraft position and found that MMS3 and MMS1 measured the same peak value of $Ve_{\perp L} \sim 160$ km/s, which decreased to $Ve_{\perp L} \sim 130$ km/s at MMS1 and to $Ve_{\perp L} \sim 60$ km/s at MMS4. Figure 3b shows that the distance between MMS1 and MMS3 in GSE Y-Z directions is less than 3 km (the size of the cubes in Figure 3b is 6.4 km). This indicates that the electron outflow tied to the X line frame was convected from MMS3 to MMS1. MMS4 separated from MMS3 by 12 km in GSE $-Z$ direction, observed a smaller $Ve_{\perp L}$. MMS2 separated from MMS3 by 17 km in GSE +Y direction observed the smallest $Ve_{\perp L}$. These multipoint velocity observations indicate that $Ve_{\perp L}$ decreases with the increasing distance from the location of the highest observed $Ve_{\perp L}$ at MMS3 and MMS1, and in accordance with Phan, Drake, et al. (2007) the width of the fast electron outflow can be about 10 km.

In Figure 7 between 00:23:49–00:23:52 and 00:23:53.5–00:23:53.7 UT fluid-scale outflows are interrupted by a short interval between 00:23:52 and 00:23:53.5 UT when no L directional perpendicular outflow is observed. However, during this time interval, B_L gets larger, that is, the distance to the current sheet increases; therefore, the spacecraft temporarily leaves the reconnection outflow channel. At the same time the spacecraft gets closer to the reconnection inflow region, which is demonstrated in Figure 7d. Here the horizontal dashed line shows the convection velocity of the stationary magnetic structure (or current sheet frame) into +N direction (Figure 3), which was estimated above to be + ~100 km/s from both MST and deHoffmann-Teller methods. The −N directional inflow is observed when $V_{\perp N} \ll 100$ km/s or negative.

From 00:23:55 to 00:23:55.2 UT and from 00:23:55.8 to 00:23:56.2 UT two −L directional perpendicular electron outflows can be seen. In between these flows $V_{\perp L} = Ve_{\perp L} = Vi_{\perp L} \sim 0$ km/s, while $B_L \sim 50$ nT. Figure 1m shows that strong pressure gradients exist in this region which can explain the enhanced bumpy magnetic field variations.

Between 00:23:54 and 00:23:55, that is, between the +L and −L directional outflows (Figure 7c) there is again a −N directional inflow (Figure 7d).

The flow structures seem to be rather complicated and of short duration, mainly between 00:23:53 and 00:23:56.5 UT. However, there are also clear consistencies, for example, the L directional perpendicular convective flows occur when the L directional parallel flows are close to zero. Also, the N directional perpendicular inflows are seen when the convective flows are absent or much smaller than the local Alfvén velocity. The occurrence of such anticorrelations indicates that despite of the short crossing times, the spacecraft are visiting physically different regions of magnetic reconnection. The proximity of the inflow-outflow regions (Norgren et al., 2016) near 00:23:53.95 UT and the occurrence of demagnetized electrons at the same time also strongly indicate that the spacecraft is near to or crossing the EDR.

Finally, Figures 7e–7g show the out-of-plane Hall term $(\mathbf{J}\times\mathbf{B}/ne)_M$ (from the generalized Ohm's law), the electric field in the moving frame of electrons $E'_M = (\mathbf{E}+\mathbf{Ve}\times\mathbf{B})_M$, and the electron temperature parallel and perpendicular to $\mathbf{B}$, $Te_{||}$, and $Te_{\perp}$, respectively. The Hall term is changing sign across the current sheet. The positive $\mathbf{E'_M}$ ensures that the plasma flows toward the X line in the inflow regions where $B_L > 0$ nT. The sharpest change in $\mathbf{E'_M}$ occurs at the position of the EDR, where electron temperature anisotropy $Te_{||} > Te_{\perp}$ is observed.

On the basis of the explanations of the processes in Figure 7 one could draw a cartoon showing the key regions of magnetic reconnection and the spacecraft trajectory across it. Before that, to achieve even a better understanding, a closer look at the EDR and at the combined structure, comprising the compressional region and electron outflow crossings, is presented in the next sections.

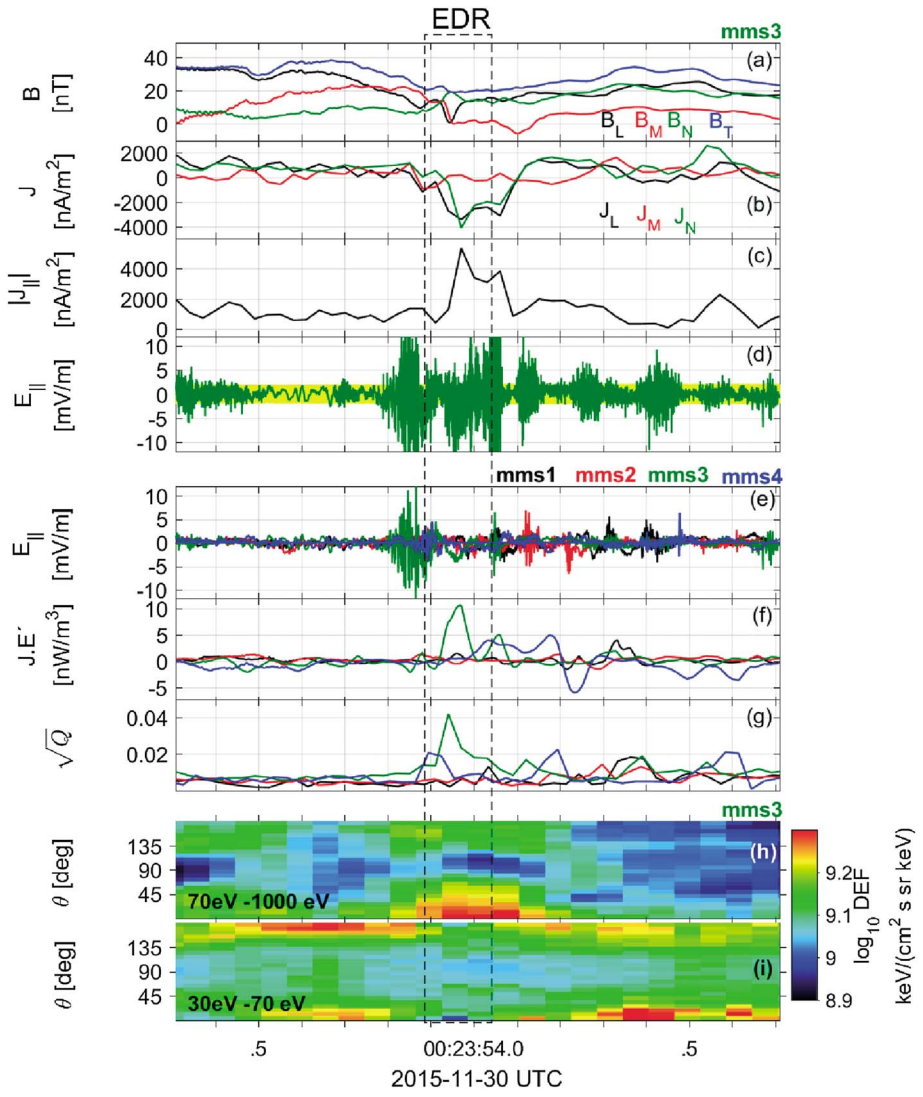

Figure 8. Crossing of the electron diffusion region (EDR) by MMS3: (a) magnetic field in LMN; (b) current density calculated from plasma data in LMN; (c) magnitude of field-aligned plasma current; (d) field-aligned electric field (green) and its errors (yellow). Observations from all spacecraft: (e) field-aligned electric field; (f) energy dissipation/conversion $J.E'$; (g) agyrotropy of the electron pressure tensor. Observations by MMS3: (h) pitch angle electron differential energy distributions in the range 70–1,000 eV; and (i) the same for the lower energy range 30–70 eV. The black dashed box highlights the EDR crossing.

6.2. Electron Diffusion Region Observation

Electron demagnetization observed after 00:23:54 UT (Figures 7c and 7d) indicates that the spacecraft are crossing an EDR. In Figure 8 more EDR signatures are presented. The EDR time interval is marked with the black dashed box between 00:23:53.66 and 00:23:53.99 UT. In the dashed box the dominant B_L and B_N magnetic components, in the vicinity of the current sheet (Figure 8a), are associated with the large J_L and J_N components (Figure 8b). These are field-aligned currents as evidenced by the magnitude of the parallel currents in Figure 8c. The high-frequency fluctuations of the parallel electric field (8,192 samples per second in Figure 8d) reach larger values than ±12 mV/m, well above the uncertainties of E field measurements (±2.5 mV/m), shown in yellow. In the vicinity and at the EDR the $E_{||}$ fluctuations are electrostatic, reaching the electron cyclotron and ion plasma frequency ranges (~1 kHz, not shown). While outside of the EDR interval the wave-like E field fluctuations are more symmetric, at the center of the EDR interval there is a clear asymmetry and the average $E_{||}$ is negative.

In Figures 8e–8g the MMS1-4 observations are compared. Figure 8e shows the resampled E field measurements (32 samples per second) with the largest $E_{||} \sim -4$ mV/m observed by MMS3 at the center of the EDR interval. This results in energy dissipation/conversion term $\mathbf{J}.\mathbf{E}' \sim 11$ nW/m^3, where $\mathbf{E}' = \mathbf{E}+\mathbf{V_e}\times\mathbf{B}$ is the electric field in the moving frame of electrons. Usually, $\mathbf{J}.\mathbf{E}'$ is called energy dissipation term, when it is positive. However, it might be difficult to show that the positive values correspond to an irreversible process, mainly when in the vicinity also negative values are observed (Figure 8f). We think, it is more safe to use the term "energy dissipation/conversion" even if $\mathbf{J}.\mathbf{E}'$ is positive. Figure 8f shows the time series of $\mathbf{J}.\mathbf{E}'$ for all four spacecraft. The positive value indicates that the energy of the magnetic field is converted/dissipated to particle kinetic and perhaps to thermal energy during magnetic reconnection. It is also expected that the gyrotropy of the electron pressure tensor $\mathbb{P}_e$ is violated near magnetic boundaries indicating locally a crossing of electron-scale layers near reconnection (Scudder & Daughton, 2008). There exists several scalar measures for quantification of the gyrotropy of $\mathbb{P}_e$. Here the agyrotropy parameter $\sqrt{Q}$ introduced by Swisdak (2016) is used. It is defined as follows:

$$Q = \frac{P_{12}^2 + P_{13}^2 + P_{23}^2}{P_{\perp}^2 + 2P_{\perp}P_{||}} \tag{4}$$

where P_{ij}s is the off-diagonal elements of $\mathbb{P}_e$. The time series of $\sqrt{Q}$ for the MMS spacecraft are shown in Figure 8g. The largest value in the EDR interval is $\sqrt{Q} \sim 0.04$.

It can be clearly seen that all these parameters are peaked at MMS3 and smaller at the other MMS spacecraft. One can ask how significant are these parameters in comparison with simulations or other observations of the EDRs. Numerical simulations of EDR in asymmetric reconnection with guide magnetic field predict $E_{||}$ of the order of 3–4 mV/m (Hesse et al., 2016). For similar boundary conditions, $E_{||} \sim 6$ mV/m was estimated in the EDR at the magnetopause (Eriksson, Wilder, et al., 2016). The energy dissipation/conversion term observed by MMS3 is close to the recently observed values $\mathbf{J}.\mathbf{E}' \sim 17$ nW/m^3 (Burch et al., 2016) and ~9 nW/m^3 (Eriksson, Wilder, et al., 2016). In numerical simulations near or at the EDR $0.03 < \sqrt{Q} < 0.2$ (Swisdak, 2016). MMS observations of asymmetric reconnection at the magnetopause found $0.05 < \sqrt{Q} < 0.16$ associated with demagnetized electrons within an electron outflow (Norgren et al., 2016). In this case, the crescent electrons were more agyrotropic. Within the magnetosheath Yordanova et al. (2016) observed $\sqrt{Q} \sim 0.055$ at the separatrix region of magnetic reconnection, however, without demagnetized electrons.

Electron pitch angle energy distributions for the energy ranges between 70–1,000 and 30–70 eV observed by MMS3 are shown in Figures 8h and 8i, respectively. Within the EDR interval the low energy field-aligned and antifield-aligned flux of electrons is reduced (Figure 8i), while the flux of high energy field-aligned electrons is increased.

Figures 8e–8g show that in terms of $E_{||}$, $\mathbf{J}.\mathbf{E}'$, $\sqrt{Q}$ the MMS3 spacecraft is the closest one to EDR. Although the magnetic field geometry can be complicated, it is possible to demonstrate that MMS3 is crossing different physical regions of magnetic reconnection than the other spacecraft. Figures 9a–9c show the four point observations of total magnetic field B_T, the B_L, and B_M components. Figure 9d shows the perpendicular components of the electron velocity $Ve_{\perp L}$, which should reach maximum values when a spacecraft is at the closest distance to the current sheet, that is, at the local minima of B_T or B_L. In fact the dashed vertical lines indicate good correlations between $Ve_{\perp L}$ maxima and B_T, B_L minima at MMS1, 2, and 3. However, after 00:23:53.9 UT only the MMS3 spacecraft observes $B_M \leq 0$ [nT] (Figure 9c). Since the reduction of the out-of-plane magnetic component or the change of its sign (there is also a guide field) is expected near the current sheet or the X line (Shay et al., 2016) the MMS3 spacecraft might be the closest one to EDR. The MMS3 spacecraft is short time in this region because the predominantly $Ve_{\perp L}$ suddenly changes to $Ve_{||L}$ at 00:23:53.94 UT (Figure 9e). The magnetic field curvature vector **curvB** was also calculated using the four point capabilities of the MMS spacecraft. Figure 9f shows the magnitude defined through $\text{curvB} = |(\mathbf{b}.\nabla)\mathbf{b}|$ where $\mathbf{b} = \frac{\mathbf{B}}{|B|}$. Figures 9d and 9f show that curvB is enhanced roughly during the time interval when $Ve_{\perp L}$ at MMS1, 2, and 3 is exceeding the local Alfvén velocity ~70 km/s. curvB ~ 0 km^{-1} corresponds to straight field lines.

Let us check the electron distributions. The electron VDFs in field-aligned coordinates (FAC) are compared at two time instants, one before and one within the EDR interval (Figures 10a–10h and 10i–10p). The FAC unit vectors are defined along the directions $V_{||}$: **B**, $V_{\perp 1}$: (**B** × **V**e) × **B**, and $V_{\perp 2}$:**B** × **V**e. Figures 10e–10g and 10m–10o show the corresponding 1-D cuts of VDFs along the major axes of the 2-D plots again for times before and within the EDR intervals, respectively. The 1-D distributions are calculated within the green

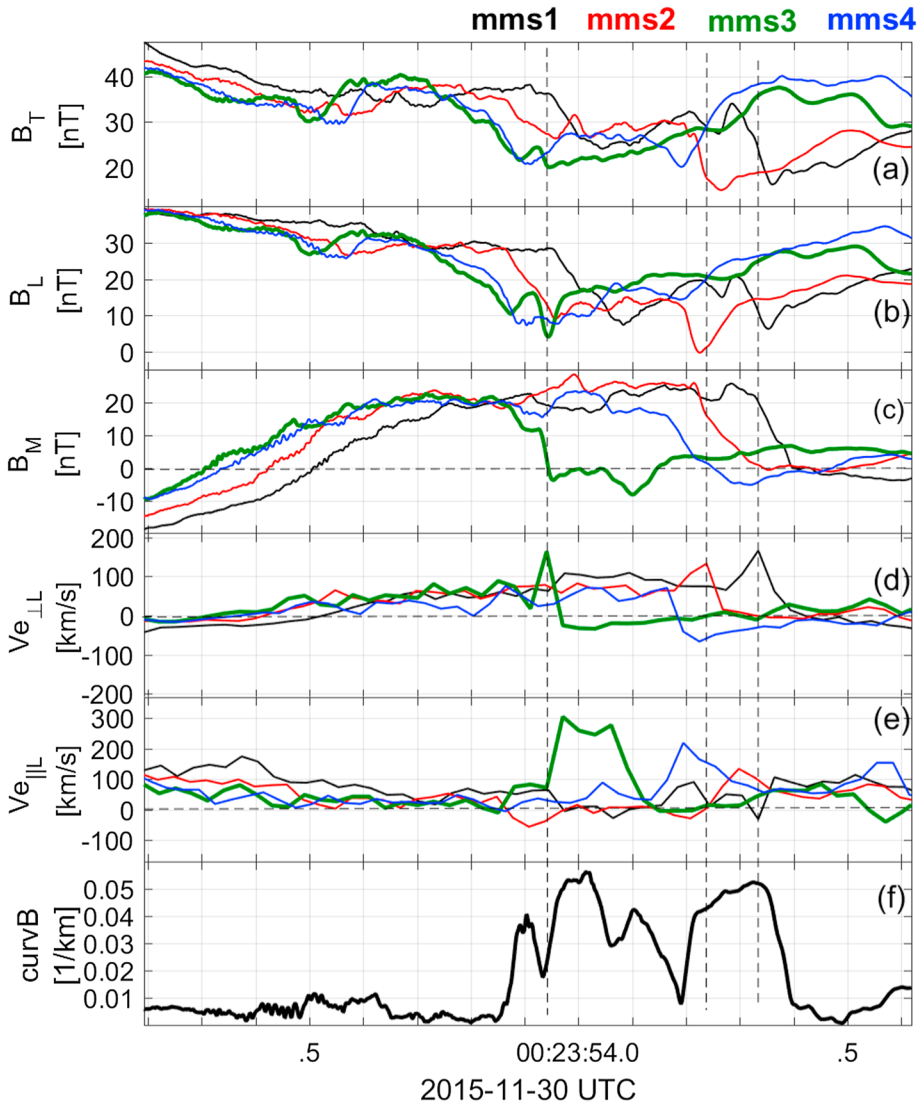

Figure 9. Four point MMS1–4 observations of (a) total magnetic field (B_T); (b) magnetic field component B_L; (c) magnetic field component B_M; (d) perpendicular L directional electron velocity $Ve_{\perp L}$; (e) parallel L directional electron velocity $Ve_{||L}$; and (f) magnitude of the magnetic curvature vector curvB = $|(\mathbf{b}.\nabla)\mathbf{b}|$ where $\mathbf{b} = \frac{\mathbf{B}}{|B|}$. The vertical dashed lines correspond to times when the peak values of $Ve_{\perp L}$ are associated with the local minima of B_T and B_L.

and black lines (positive velocities) and dashed lines (negative velocities) shown in 2-D VDFs. The core of the electron VDFs represents a flat-top distribution, which is readily discernible from the 1-D cuts. In the perpendicular directions ($V_{\perp 1} - V_{\perp 2}$, top panels) the asymmetry of the VDF within the EDR (Figures 10i and 10m) compared to the more symmetric case outside of the EDR (Figures 10a and 10e) is clearly seen. This asymmetry is quantified by the scalar agyrotropy parameter reaching $\sqrt{Q} \sim 0.04$. We believe that the relatively small $\sqrt{Q}$ or asymmetry indicate that MMS3 is not crossing the central part of the EDR but skimming the outer region of it. The ratios $f(v_{\perp 1})/f(v_{\perp 1})$ and $f(-v_{\perp 1})/f(-v_{\perp 1})$ (Figures 10h and 10p) indicate that the enhanced agyrotropy within EDR (Figure 10p) is associated with suprathermal electrons. The vertical magenta line corresponds to the thermal velocity V_{therm} in the bottom panels. In Figures 10b, 10c, 10f, 10g, 10j, 10k, 10n, and 10o the electron VDFs for $V_{||} - V_{\perp 1}$ and $V_{||} - V_{\perp 2}$ are compared, respectively. Within the EDR (right panels) the anisotropy or elongation in the parallel direction is clearly seen. The ratios of $f(v_{||})/f(-v_{||})$ (Figures 10d and 10l) show a peak >1 at V_{therm}; however, the ratio is <1 at the suprathermal range. Similar asymmetric and anisotropic electron VDFs exist during the whole interval near 00:23:54 UT, when $Te_{||} > Te_{\perp}$ (Figure 7g), electron demagnetization occurs and $E_{||}$, $J.E'$ and $\sqrt{Q}$ are enhanced (Figure 8). Before and after the region highlighted with the black dashed box, MMS3 is in the IDR.

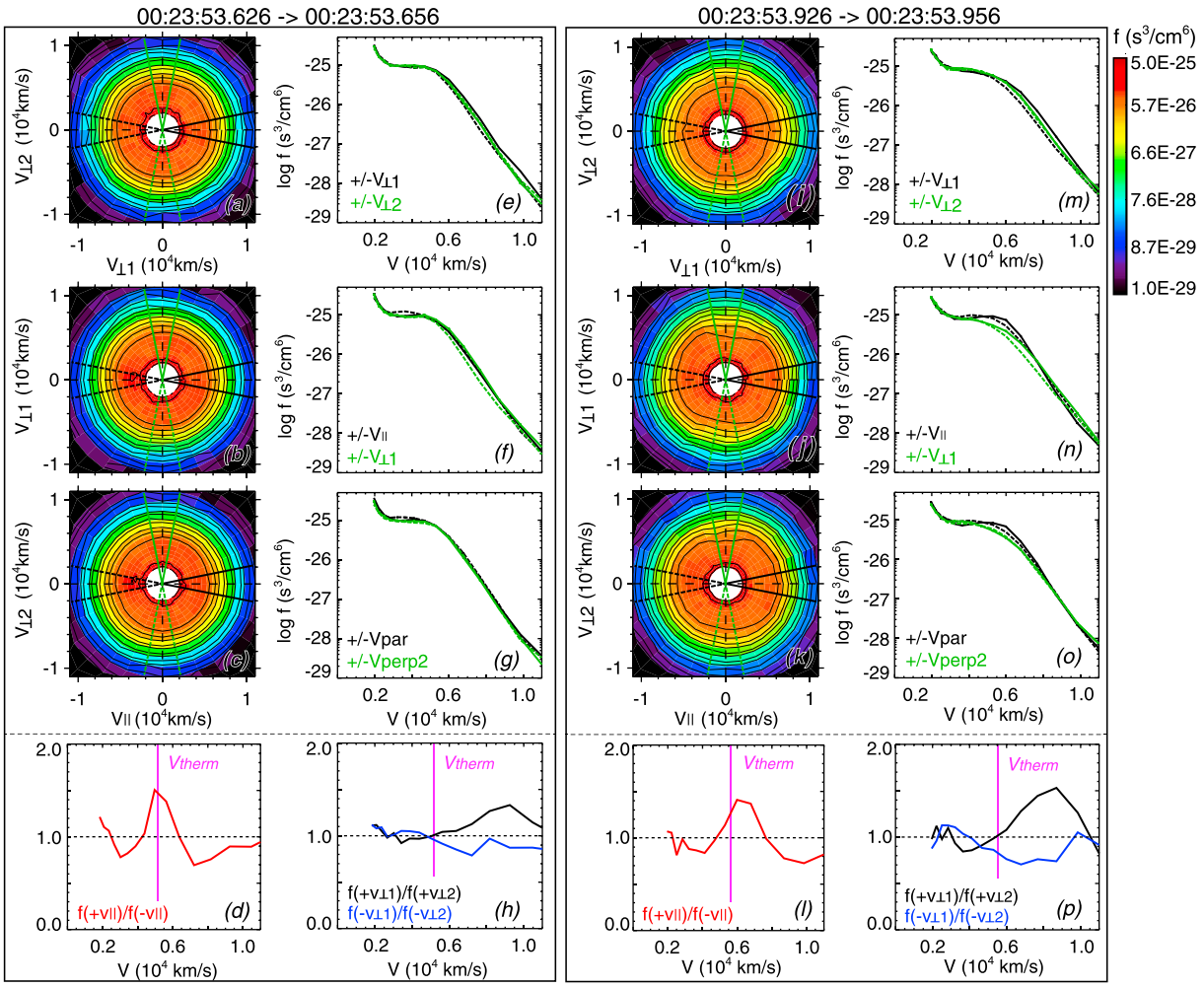

Figure 10. MMS3 observations of 2-D and 1-D cuts of electron velocity distribution function (VDF). (a–h) VDFs outside of EDR. (i–p) Inside of the EDR. The 2-D cuts are in field-aligned coordinates (FAC): $V_{\perp 1}$-$V_{\perp 2}$ (Figures 10a and 10i), ($V_{||}$-$V_{\perp 1}$) (Figures 10f and 10n), and in $V_{||}$-$V_{\perp 2}$ (Figures 10g and 10o) planes. The 1-D cuts (Figures 10e–10g and 10m–10o) are obtained along the major axis of 2-D plots within the dashed and solid lines. Bottom plots: ratios of $f(v_{||})/f(-v_{||})$, $f(v_{\perp 1})/f(v_{\perp 1})$ and $f(-v_{\perp 1})/f(-v_{\perp 1})$. $V_{\mathrm{therm}} = 5,200$ km/s (vertical magenta line) is the thermal velocity.

6.3. Crossing of Electron Outflows and the Current Sheet

Between 00:23:53.8 and 00:23:55.2 UT MMS3 is in the IDR (Figures 7c and 7d) and at the end of this time interval the first electron outflow is seen (Figure 7c). After the electron outflow B_T and B_L increase to 50 and later to 60 nT (Figure 11). The dashed lines in Figure 11a show a constant twist flux rope model fit to the magnetic field data (Gold & Hoyle, 1960). The axial field is B_L, and it reaches its maximum close to the time instant when the bipolar azimuthal field B_M goes through zero. Figure 11b shows that there is a field-aligned current J_L reaching ~−2,000 nA/m^2 which can be associated with the magnetic twist. Immediately after, starting at 00:23:55.8 UT the magnetic field rotates and at the same time a second electron outflow is seen in Figure 7c. Both −L directional electron outflows are associated with negative B_N. Additionally, the rotation of the magnetic field associated with Hall magnetic field $B_M = -30$ nT (−15 nT guide field) and with the sign changing J_L (Figure 11b) and Hall electric field E_N (Figure 11c) together with $-B_N$ indicate that the spacecraft cross the current sheet south of the X line in −N direction. Figure 11d shows an increasing density across the current sheet implying possible asymmetric boundary conditions for the ongoing reconnection. Similar one-dimensional profiles of field and current components along an N directional crossing of the current sheet at a distance of 6.35 d_i from the X line were identified in kinetic particle-in-cell simulations of asymmetric reconnection (Shay et al., 2016).

The flux rope can be positioned roughly at the magnetic separatrix region. This observation is not exceptional, a flux rope at the separatrix region of magnetic reconnection occurring in the Earth's magnetotail

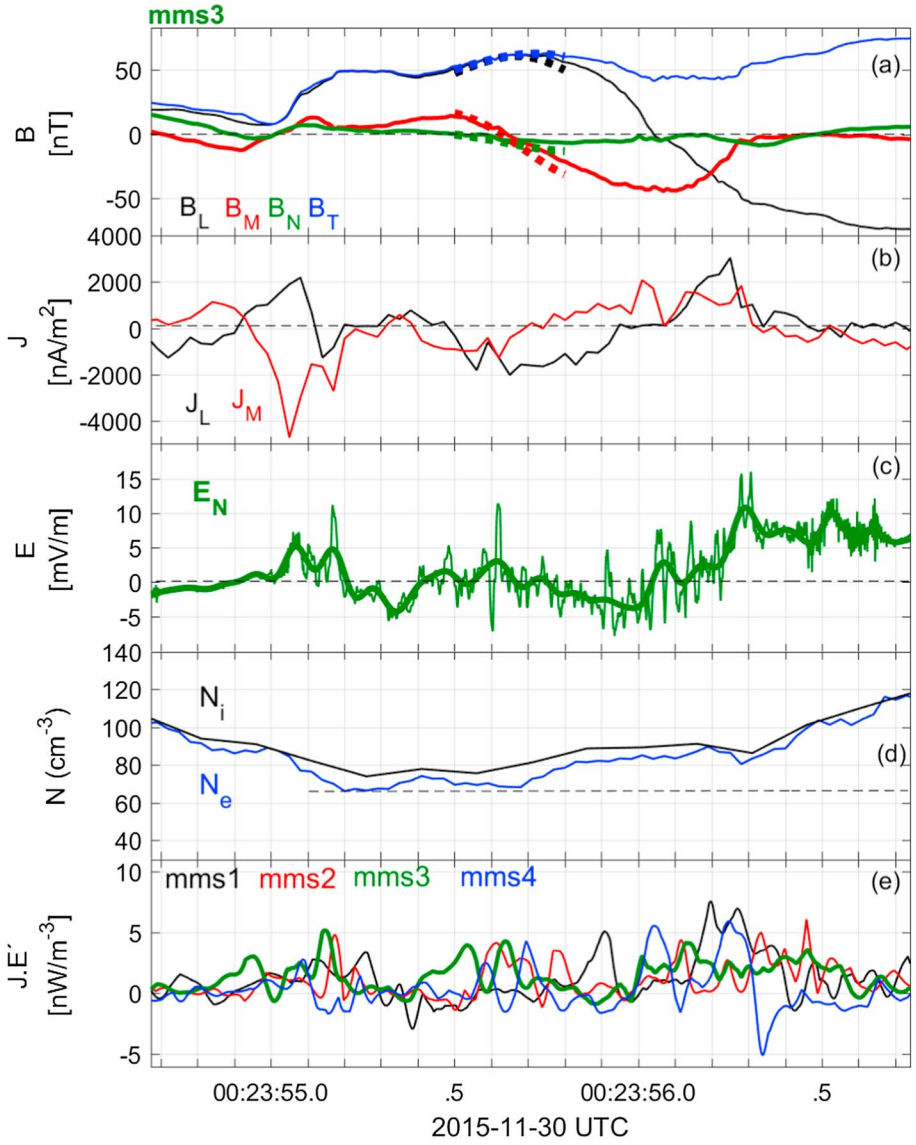

Figure 11. Crossing of the current sheet and a flux rope: (a) Magnetic field in LMN. The dashed thick lines represent local fits of the constant twist flux rope model; (b) current density L and M components calculated from the plasma data; (c) normal component of the electric field (thin green line) and the smoothed E_N (thick green line); and (d) ion and electron densities. The dashed horizontal line guides the eyes to see how the density increases across the current sheet; and (e) energy dissipation/conversion term $\mathbf{J}.\mathbf{E}'$ for all four spacecraft.

has already been observed by Cluster (Huang et al., 2016). Anyhow, in our case, the crossing of the magnetic field compressional region and of a possible flux rope occurs outside of the electron outflow channel, at a larger distance from the current sheet. This can be the reason why two separated electron outflows are seen, interrupted during the enhanced magnetic field in the middle. Figure 11e shows $\mathbf{J}.\mathbf{E}'$ for this time interval. While the dissipation/conversion term is nonnegligible, the agyrotropy is small ($\sqrt{\mathbf{Q}}$ not shown).

Finally, the magnetic jump, best seen in B_T at 00:23:56.28 UT, was considered as a potential MHD discontinuity. This structure is observed by each MMS spacecraft (Figure 4a) and separates the reconnection outflow from the high-density, low ion temperature and elevated total pressure structure seen between the right-hand borders of dashed blue and black boxes in Figure 1. The MVA analysis gives approximately the same normal directions for all MMS spacecraft, for example, for MMS3 $\mathbf{N}[-0.97 \quad 0.12 \quad -0.20]$ GSE with ratios $r_{12} \sim 31$ and $r_{23} \sim 36$. However, the best eigenvalue ratios are obtained for a rather short time interval of ~0.02 s, which is converted to space ~2 km~ $4d_e \ll d_i$ (d_e is the electron inertial length). The normal directions of the magnetic jump structure are very similar to the **N** direction of the current sheet. In order to check if the jump structure

resembles a tangential discontinuity (TD) the B, V_i, and V_e vectors were projected to the N direction of jump structure. For MMS3 $\langle B_N \rangle \sim -1.5$ nT, $\langle Vi_N \rangle \sim 2$ km/s and $\langle Ve_N \rangle \sim -30$ km/s. According to Sonnerup and Scheible (1998) a composite statistical error can be calculated to evaluate if $\langle B_N \rangle$ is close enough to zero to be classified as a TD. Using their criteria, we obtained $\langle \delta B_N \rangle = 1.1$ nT, which is very close to $|\langle B_N \rangle|$. This shows that the normal component of the magnetic field can be considered zero across the discontinuity. Regarding the plasma flows across the discontinuity, $\langle Vi_N \rangle$ is negligible, while $\langle Ve_N \rangle$ is not, it is about 20% of the magnitude of $\langle Ve \rangle$. In summary, the magnetic jump structure resembles a TD, but it is of kinetic scale rather than of fluid scale and there is a nonnegligible electron flow across it. It may then be safer to call this type of boundary a kinetic-scale nonlinear structure (Balikhin et al., 2014). The reconnection associated $Ve_{||L}$ spikes end at this boundary (Figure 7b).

7. Reconnection and Spacecraft Trajectory Geometries

Figure 12 shows a cartoon of the reconnection and spacecraft trajectory geometries reconstructed from the observations and on the basis of interpretations offered in previous sections. The LMN coordinate system is shown on top left, the GSE X directional spacing between the MMS1-4 spacecraft on top right. The MMS3 spacecraft trajectory across the reconnection region is shown by the green dashed line from north (+L) to south (−L) directions. The EDR and IDR regions are represented by the filled violet and light brown boxes, respectively. The electron outflows (inside the IDR) and the MHD-scale outflows (outside of IDR) in both ±L directions are indicated by the filled arrows. Despite the fact that there is a significant guide field and asymmetry between the upstream and downstream regions we keep the standard symmetric 2-D shape of the reconnection scheme with the only distortion of the small flux rope at the bottom left corner of IDR. The trajectory of the spacecraft is complicated, supposedly due to irregular motions, even small rotations or deformations of the underlying structures. Since detailed simulation results for guide field asymmetric reconnection events embedded into a turbulent environment do not exist, we feel that a cartoon as simple as possible is a reasonable choice. One has to keep in mind that while the local variables consistently describe the distinct reconnection regions, the physical scales indicated in the cartoon might be slightly disproportional.

Let us recapitulate shortly the observations from the previous sections by indicating the corresponding locations in the cartoon (Figure 12). To help orientation, there are four locations in the cartoon indicated by red-green points (1)–(4) on the trajectory of MMS3. We will alternately refer to a location in the cartoon and the data presented in previous sections. The MMS3 spacecraft enters from the upstream region through a RD-like boundary to the reconnection outflow region (top right — location (1)). Here positive B_L and B_N components are observed; therefore, the reconnection X line is south from this location. Accordingly, +L directional perpendicular outflows are seen (Figures 7a and 7c). In between two outflows B_L becomes larger, MMS3 gets closer to the inflow region (between location (1) and the right edge of IDR), where the $+E_M$ directional tangential electric field and the northward $+B_L$ ensure the −N directional convective inflow $-V_{\mathrm{IN}}$ (roughly between 00:23:52 and 00:23:53.5 UT in Figures 7a, 7d, and 7f). Then MMS3 gets again closer to the current sheet ($+B_L$ decreases) and by going closer to the X line first an ion-electron outflow, then a very short electron outflow is seen at the blue dashed vertical line in Figure 7 (between top right corners of IDR and EDR). Then the MMS3 spacecraft skims the outer region of the EDR (Figures 8 and 14, before location (2) in EDR). The other MMS probes are more Earthward and therefore do not approach the EDR. After a short time MMS3 appears again in the inflow region (increased $+B_L$, $+E_M$) within the IDR (between 00:23:54 and 00:23:55 UT in Figures 7a–7d, upstream from the X line). After 00:23:55 UT both negative L directional perpendicular electron outflows inside IDR are associated with negative B_N (Figures 7a, 7c, and 11a), indicating that the spacecraft is south from the X line (locations (3–4). In between the $-Ve_{\perp L}$ outflows a short excursion outside the IDR to the flux rope region is observed where first positive then negative out-of-plane B_M is seen which is associated with the magnetic twist of the flux rope with axis orientation roughly in L direction (between locations (3) and (4)). In Figure 12 the flux rope is placed to the separatrix; however, it would not change the interpretation if it was positioned farther out, more into the inflow region. The crossing of the current sheet is again across the IDR where the second electron outflow (location (4)) is observed. At the left bottom position MMS3 is crossing a TD-like kinetic nonlinear boundary, leaving the reconnection structure behind. The Hall electric field is negative at the upstream $+B_L$ and positive at the downstream $-B_L$ positions (Figures 11a and 11c). Supposing perpendicular crossing the cross-sectional size of the outflow region is $\sim 3d_i = 75$ km.

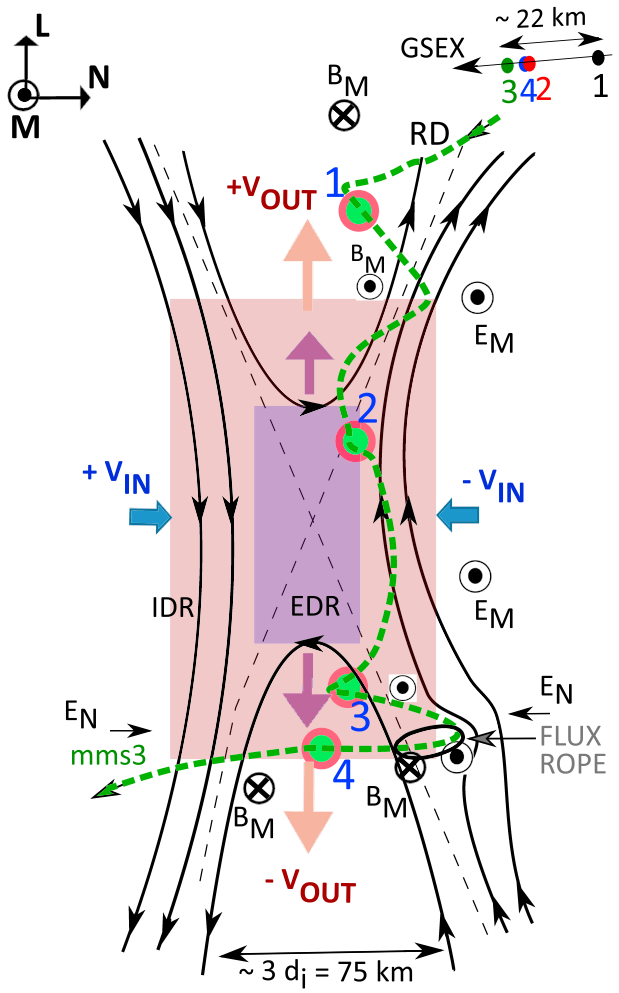

Figure 12. The quasi 2-D geometry of the magnetic reconnection. The LMN coordinates are shown in top left, the GSE distances of MMS probes in top right corners. The green dashed line shows MMS3 trajectory across reconnection. The red-green circles 1 ÷ 4 are reference points. RD stays for rotational discontinuity. The light brown and violet boxes depict the IDR and EDR, respectively. The thick arrows show the outflows and the inflows. E_M is the out-of-plane tangential electric field. E_N and B_M are the Hall electric and magnetic fields. The deformation in the field lines close to the left bottom edge of the IDR is due to an embedded small-scale flux rope.

The changing sign of the out-of-plane B_M magnetic field is indicated along the trajectory of MMS3. Relative to the guide field (Figure 4c) B_M is predominantly positive closer to the upstream and negative closer to the downstream region of reconnection. It is difficult to identify any bipolar or quadrupolar Hall magnetic structure. However, the distribution of B_M in kinetic simulations of reconnection around the X line is also nontrivial (Shay et al., 2016). Moreover, during the vertical crossing of the reconnection region the whole structure undergoes complicated motions and the spacecraft can visit regions with locally prevailing $\pm B_M$.

Now with the known reconnection geometry we can estimate the magnetic shear angle Θ_{SH} between a few magnetic field vectors in the upstream and downstream regions. We chose a reference point in the downstream region at 00:23:56.7 UT and starting at 00:23:49.00 ending at 00:23:55.90 UT; we calculated Θ_{SH} for MMS3 in several points along the L direction in the upstream region. Θ_{SH} changes between 140° and 170°, the largest value is obtained between vectors at the beginning and end of the largest field rotation. The result is the same for the other spacecraft, too. Obviously, Θ_{SH} can change along L direction in time as well, but in comparison, the values between 140° and 170° correspond to the largest observed magnetic shears in the solar wind (Phan et al., 2010). The difference between average upstream-downstream plasma β in the immediate vicinity of the largest Θ_{SH} is $\Delta\beta \sim 1$. On this basis, there is a good chance that the reconnection is not suppressed.

8. Kinetic Signatures of Reconnection

Using the cartoon of Figure 12 and the (1)–(4) reference points (red-green circles) in it, now we can also demonstrate the occurrence of ion kinetic signatures of magnetic reconnection within the reconnection outflow (location (1)) and inside the IDR (location (2)). Furthermore, we present electron VDFs at the locations (3) and (4) of perpendicular electron outflows $-Ve_{\perp L}$ to ascertain that these low-amplitude flows are indeed associated with convective motion of electrons. We believe that besides the above presented signatures of EDR crossing (northward of location (2)), the kinetic evidence for the occurrence of magnetic reconnection is rather strong.

Figures 13a–13c show the VDF cuts of the ion distribution functions at 00:23:51.51 UT (location (1) in Figure 12). This is the location in the reconnection outflow region ($+V_{OUT}$), where significant perpendicular convective $Vi_{\perp L}$, $Ve_{\perp L}$ flows are observed (Figure 7c). The observations of MMS3 are presented in Figures 13a–13c. Figure 13a demonstrates a cut of VDF in $V_{E\times B}$-V_B plane, Figure 13b the VDF cut in V_B-V_E plane, and Figure 13c ion energy distributions for three different pitch angles 0°, 90°, and 180°. From the VDF cuts, it is evident that the core population of the ions is not isotropic, but instead, it exhibits a cutoff in antifield-aligned direction, creating a D shape distribution. A relevant anisotropy is also evident from Figure 13c, where the highest flux is carried by the field-aligned population (pitch angle 0°). This D shape ion distribution is a well-known feature of reconnection, and the results of the observation of the population injected onto the reconnected field lines (Cowley, 1995). Note that the D shape is more symmetrically observed in Figure 13b, as the cut is not in the plane affected by the convection of the population. While in Figure 13a the whole D shape is shifted to the right, in $\mathbf{E}\times\mathbf{B}$ direction, which corresponds to the convection direction of ions. This type of ion VDFs is observed everywhere in the outflow region outside of IDR.

In Figures 13d–13f, the same set of plots are shown for MMS3 observation at 00:23:54.21 UT, which is also marked as point (2) in Figure 12. It is immediately clear that there is a significant difference between the VDF cuts in Figures 13d and 13e and those in Figures 13a and 13b. The VDF cut in $V_{E\times B}$-V_B plane consists of two

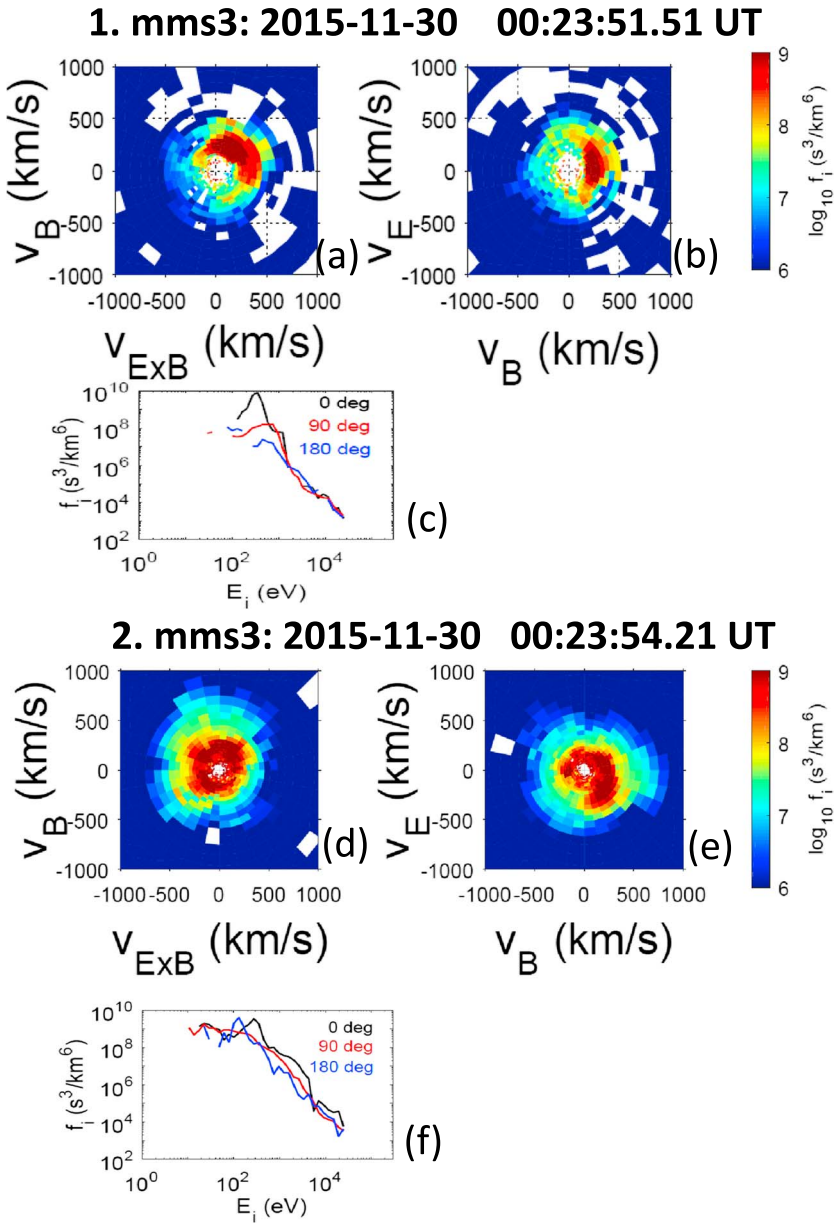

Figure 13. Ion VDFs measured by MMS3 in locations (1) and (2) in Figure 12. (a–c) D shape ion VDFs within reconnection outflow in location (1). (a) Ion VDFs cuts in $V_{E\times B}$-V_B plane; (b) in V_B-V_E plane; and (c) ion energy distributions for pitch angles 0°, 90°, and 180°. (d–f) Crescent ion VDFs within the IDR in location (2). Notation is the same as in the subplots a–c.

crescent-like distributions of ions in field-aligned and antifield-aligned direction, with slightly different temperature. This observation is consistent with the ion energy distribution in Figure 13f where the peak of black trace line (pitch angle 0°) has higher energy than that of blue trace line (pitch angle 180°). The VDF cut in V_B-V_E plane, Figure 13e, shows that the relatively hotter field-aligned population is elongated in **E** direction. These observations are suggestive of mixing between two different ion populations via reconnection. Similar observations of two/multiple distinct populations of ions, with asymmetric distribution in **E** direction, are indicative of IDR (Nagai et al., 2015; Yordanova et al., 2016; Zhou et al., 2009). In fact, we get similar ion VDFs inside IDR.

We now look into the distribution of electrons in the outflow region. We mention that similarly to the cases in Figure 10 the electron VDFs form again top-hat core distributions and the color codes used below are optimized to see the high energy portion of VDFs. Figures 14a and 14b show the $V_{E\times B}$-V_B plane VDF cuts of the

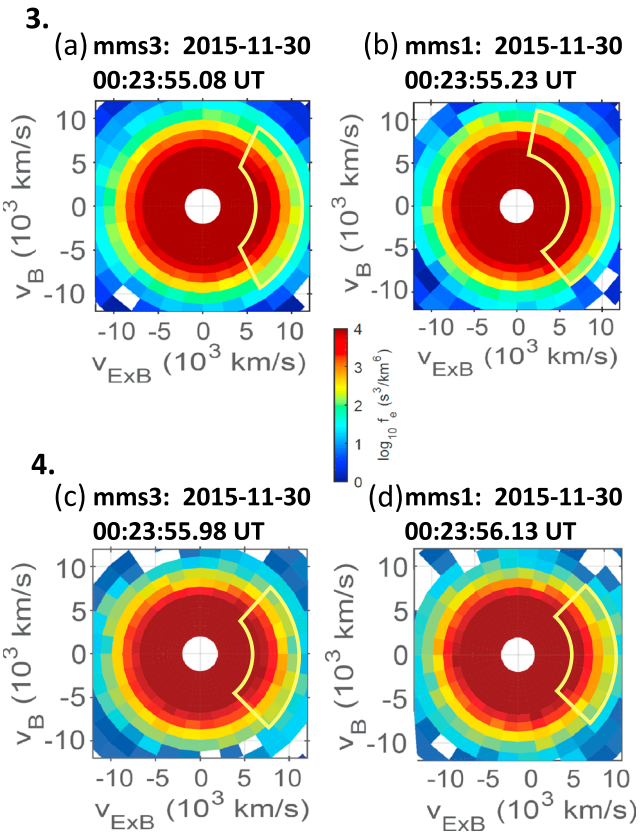

Figure 14. Electron VDF cuts in V_{ExB}-V_B plane measured by MMS3 and MMS1 in locations (3) and (4) in Figure 12. Top panels: electron VDFs in location (3) inside the first perpendicular electron outflow; (a) MMS3 measurements; (b) MMS1 measurements. Bottom panels: electron VDFs in location (4) inside the second perpendicular electron outflow; (c) MMS3 measurements; (d) MMS1 measurements. The yellow fans closed lines mark the enhanced flux along the **E** × **B** direction.

electron distribution function observed by (a) MMS3 at 00:23:55.08 UT and by (b) MMS1 at 00:23:55.23 UT (location (3) in Figure 12). This is the location in the reconnection outflow region ($-V_{OUT}$), where perpendicular convective $-Ve_{\perp L}$ flows are observed (Figure 7c).

Figures 14c and 14d show the V_{ExB}-V_B plane VDF cuts of the electron distribution function observed by (c) MMS3 at 00:23:55.98 UT and by (d) MMS1 at 00:23:56.13 UT (location (4) in Figure 12). This is the location of the second electron outflow ($-V_{OUT}$), where perpendicular convective $-Ve_{\perp L}$ flows are observed again (Figure 7c). From the four panels in Figure 14, it is evident that the magnetosheath colder electrons covering the dark brown pixels below 4,000 km/s are mostly isotropic. However, for the hotter electron population (>4,000 km/s) there is more flux observed on the right side of the VDF rings, along the **E** × **B** direction. To demonstrate this better, the hotter portion of the population is marked by the yellow fan closed lines in each panel. These populations are the main contributors to the electron jets shown in Figure 7c.

9. Discussion and Conclusions

The main goal of this paper was to provide a detailed structure of a magnetic reconnection event in the turbulent magnetosheath downstream of a QPar bow shock. A candidate event was found on the basis of identification of discontinuities, current sheets, local acceleration of particles or heating of plasma (Figure 1). Recent simulations of plasma turbulence predict the generation of these structures, including reconnecting current sheets, by turbulent motions and self-organization via multiscale redistributions of the available free energy. The chosen magnetosheath event was also associated with ion and electron bulk flows which we expected to be reconnection generated.

The first challenge was to find a proper LMN coordinate system in which the supposedly quasi-2-D reconnection ideas would be exploitable. Although the turbulent magnetosheath is expected to be a fully 3-D plasma system, the 2-D geometry, as a first attempt of study turbulence generated structures, would significantly help to interpret the data by comparing it to the 2-D reconnection studies at large-scale boundaries (magnetopause, magnetotail current sheet). In the end the LMN eigenvectors were obtained from MVA analysis of magnetic field during a time interval of short crossing of the entire current sheet (<1 s) with the largest rotation of the magnetic field. The MVA coordinates estimated at the four MMS spacecraft locations were similar. Furthermore, within the estimated uncertainties, the normal direction from the multipoint MST method was the same as from MVA. The MST method also allowed to estimate the time shifts between the structures seen by the MMS spacecraft over the whole period of interest (~8 s, Figures 2 and 7), and it was found that the time shifts remained roughly the same. This implied that, possibly, the LMN system was valid for a longer time interval, not only for the short time interval of MVA. Indeed, the existence of the deHoffmann-Teller frame in which the convection electric field vanishes indicated that there exists a quasi-stationary magnetic field structure which moves toward the Earth (N direction, roughly −XGSE) but also has significant velocity components in −Y and +Z GSE directions (roughly +L direction, Figure 3). This motion resulted in a complex trajectory across the whole structure along which both ±L directional reconnection outflows and the −N directional plasma inflow could be seen (Figure 12). The normal speeds of the current sheet obtained from MST and deHoffmann-Teller analyses were approximately the same. We found that the analysis of the reconnection event in the chosen LMN system is consistent. For example, the field, plasma and particle signatures of EDR crossing were observed when the relative values of the LMN magnetic field components and the spatial proximity of LMN inflow and outflow velocities indicated that the spacecraft were in the closest position to the current sheet and the X line. The LMN system is also not perfect. The background plasma and fields are inhomogeneous; there exists substructures (a flux rope) and local compressions, which can deform and move the whole reconnection structure leading to an irregular trajectory (Figure 12).

The fluid-scale signatures of magnetic reconnection were tested in the deHoffmann-Teller frame by invoking the Walén test. The scatterplots between the Aflvén speed and ion/electron velocity components showed the expected level of correlations, indicating that the deHoffmann-Teller frame is well defined for the time interval of reconnection crossing. Since the changes of the sign of regression slopes were associated with the change of the sign of B_N the MMS spacecraft crossed both sides of the reconnection X line. Figure 12 shows that the +L directional outflow was bordered by a RD, but the entire outflow was not crossed. In the −L direction the MMS3 spacecraft observed electron perpendicular outflow only, and the downstream border of the outflow was a nonlinear narrow kinetic structure. This is certainly indicating that kinetic structures were crossed along the trajectory as well, for which the fluid description is not valid. Although we do not consider the results of the Walén test as an ultimate proof for reconnection, the test certainly demonstrates that over the time interval of interest (Figure 4) Alfvénic correlations exist in the deHoffmann-Teller frame, which disappear when longer time intervals are examined.

Similarly to previous studies (Phan, Paschmann, et al., 2007; Retinò et al., 2007; Yordanova et al., 2016), we also found that the evidence for ongoing reconnection comes from the observations of the following: (1) reconnection inflows and outflows with proper sign of B_N, (2) out-of-plane tangential electric field, (3) Hall electric and magnetic fields, (4) particle acceleration, heating, and demagnetization, and (5) energy dissipation/conversion.

Additionally, in our event, one spacecraft crossed both IDR and EDR. D shape ion VDFs were observed in the reconnection outflow region where both ions and electrons were magnetized. In the IDR typical VDFs of demagnetized ions were observed with mixing of different ion populations energized also by the electric field. Within the EDR the parallel electric field was associated with energy dissipation/conversion ($\mathbf{J}.\mathbf{E}' > 0$), electron agyrotropy, electron temperature anisotropy, and electron heating. All these observations represent the kinetic signatures of an ongoing magnetic reconnection, which have been observed for the first time in the turbulent magnetosheath.

Finally, we mention that it is relatively easy to find the current sheets in the turbulent magnetosheath. However, it is rather nontrivial to prove that the current system is actually associated with ongoing reconnection. It might be always a challenge to find a proper coordinate system or to identify the small amplitude Alfvénic outflows at the vicinity of X lines, and treat the underlying structures which are not always in pressure balance. It is also obvious that the fluid description has its limitations, the Walén test might fail, and the boundaries are kinetic nonlinear structures rather than MHD discontinuities. In this respect, the vast majority of the reconnection events in a turbulent environment can be overlooked.

Acknowledgments
Z. V. was supported by the Austrian Fond zur Förderung der wissenschaftlichen Forschung (FWF projects P24740-N27 and P28764-N27). E. Y. was supported by the Swedish Civil Contingencies Agency, grant 171/16. French involvement (SCM instruments) on MMS is supported by CNES, CNRS-INSIS, and CNRS-INSU. The data used in this paper are freely available from the MMS data center: https://lasp.colorado.edu/mms/sdc/public/.

References

Balikhin, M. A., Runov, A., Walker, S. N., Gedalin, M., Dandouras, I., Hobara, Y., & Fazakerley, A. (2014). On the fine structure of dipolarization fronts. *Journal of Geophysical Research: Space Physics*, *119*, 6367–6385. https://doi.org/10.1002/2014JA019908

Burch, J. L., Torbert, R. B., Phan, T. D., Chen, L.-J., Moore, T. E., Ergun, R. E., … Chandler, M. (2016). Electron-scale measurements of magnetic reconnection in space. *Science*, *352*, AF2939. https://doi.org/10.1126/science.aaf2939

Burgess, D, Lucek, E. A., Scholer, M., Bale, S. D., Balikhin, M. A., Balogh, A., … Walker, S. N. (2005). Quasi-parallel shock structure and processes. *Space Science Reviews*, *118*, 205–222. https://doi.org/10.1007/s11214-005-3832-3

Carbone, V., Veltri, P., & Mangeney, A. (1990). Coherent structure formation and magnetic field line reconnection in magnetohydrodynamic turbulence. *Physics of Fluids A*, *2*(8), 1487–1496. https://doi.org/10.1063/1.857598

Cowley, S. W. H. (1995). Theoretical perspectives of the magnetopause: A tutorial review. In P. Song, B. U. Ö. Sonnerup, & M. F. Thomsen (Eds.), *Physics of the magnetopause, Geophysical Monograph Series* (Vol. 90, pp. 29–43). Washington, DC: American Geophysical Union.

Chao, J. K., Hsieh, W. C., Yang, L., & Lee, L. C. (2014). Walén test and de deHoffmann-Teller frame of interplanetary large-amplitude Alfvén waves. *The Astrophysical Journal*, *786*, 149. https://doi.org/10.1088/0004-637X/786/2/149

Chasapis, A., Matthaeus, W. H., Parashar, T. N., Le Contel, O., Retinò, A., Breuillard, H., … Saito, Y. (2017). Electron heating at kinetic scales in magnetosheath turbulence. *The Astrophysical Journal*, *836*, 247. https://doi.org/10.3847/1538-4357/836/2/247

Chasapis, A., Retinò, A., Sahraoui, F., Vaivads, A., Khotyaintsev, Y. V., Sundkvist, D., … Canu, P. (2015). Thin current sheets and associated electron heating in turbulent space plasma. *The Astrophysical Journal Letters*, *804*, L1. https://doi.org/10.1088/2041-8205/804/1/L1

Dunlop, M. W., Balogh, A., Glassmeier, K.-H., & Robert, P. (2002). Four-point Cluster application of magnetic field analysis tools: The Curlometer. *Journal of Geophysical Research*, *107*(A11), 1384. https://doi.org/10.1029/2001JA005088

Ergun, R. E., Tucker, S., Westfall, J., Goodrich, K. A., Malaspina, D. M., Summers, D., … Cully, C. M. (2016). The axial double probe and fields signal processing for the MMS mission. *Space Science Reviews*, *199*, 167–188. https://doi.org/10.1007/s11214-014-0115-x

Eriksson, E., Vaivads, A., Graham, D. B., Khotyaintsev, Y. V., Yordanova, E., Hietala, H., … Burch, J. (2016). Strong current sheet at a magnetosheath jet: Kinetic structure and electron acceleration. *Journal of Geophysical Research: Space Physics*, *121*, 9608–9618. https://doi.org/10.1002/2016JA023146

Eriksson, S., Wilder, F. D., Ergun, R. E., Schwartz, S. J., Cassak, P. A., Burch, J. L., … Marklund, G. T. (2016). Magnetospheric multiscale observations of the electron diffusion region of large guide field magnetic reconnection. *Physical Review Letters*, *117*, 15001. https://doi.org/10.1103/PhysRevLett.117.015001

Feng, H., & Wang, J. (2013). Magnetic-reconnection exhausts in the sheath of magnetic clouds. *Astronomy and Astrophysics*, *559*, A92. https://doi.org/10.1051/0004-6361/201322522

Fischer, D., Magnes, W., Hagen, C., Dors, I., Chutter, M. W., Needell, J., … Baumjohann, W. (2016). Optimized merging of search coil and fluxgate data for MMS. *Geoscientific Instrumentation, Methods and Data Systems*, *5*, 521–530. https://doi.org/10.5194/gi-5-521-2016

Gary, S. P., Li, H., O'Rourke, S., & Winske, D. (1998). Proton resonant firehose instability: Tempearute anisotropy and fluctuating field constraints. *Journal of Geophysical Research*, *103*(A7), 14,567–14,574.

Gold, T., & Hoyle, F. (1960). On the origin of solar flares. *Monthly Notices of the Royal Astronomical Societ*, *120*, 89. https://doi.org/10.1093/mnras/120.2.89

Goldman, M. V., Lapenta, G., Newman, D. L., Markidis, S., & Che, H. (2011). Jet deflection by very weak guide fields during magnetic reconnection. *Physical Review Letters*, *107*, 135001. https://doi.org/10.1103/PhysRevLett. 107.135001

Gosling, J. T. (2012). Magnetic reconnection in the solar wind. *Space Science Reviews*, *172*, 187–200. https://doi.org/10.1007/s11214-011-9747-2

Gosling, J. T., Skoug, R. M., McComas, D. J., & Smith, C. W. (2005). Direct evidence for magnetic reconnection in the solar wind near 1 AU. *Journal of Geophysical Research*, *110*, A01107. https://doi.org/10.1029/2004JA010809

Greco, A., Chuychai, P., Matthaeus, W. H., Servidio, S., & Dmitruk, P. (2008). Intermittent MHD structures and classical discontinuities. *Geophysical Research Letters*, *35*, L19111. https://doi.org/10.1029/2008GL035454

Greco, A., Matthaeus, W. H., Servidio, S., Chuychai, P., & Dmitruk, P. (2009). Statistical analysis of discontinuities in solar wind ACE data and comparison with intermittent MHD turbulence. *Astrophysics Journal*, *691*, L111–L114. https://doi.org/10.1088/0004-637X/691/2/L111

Hellinger, P., & Trávníček, P. (2006). Parallel and oblique proton fire hose instabilities in the presence of alpha/proton drift: Hybrid simulations. *Journal of Geophysical Research*, *111*, A01107. https://doi.org/10.1029/2005JA011318

Hellinger, P., Trávníček, P., Kasper, J. C., & Lazarus, A. J. (2006). Solar wind proton temperature anisotropy: Linear theory and WIND/SWE observations. *Geophysical Research Letters*, *33*, L09101. https://doi.org/10.1029/2006GL025925

Hesse, M., Neukirch, T., Schindler, K., Kuznetsova, M., & Zenitani, S. (2016). The diffusion region in collisionless magnetic reconnection. *Space Science Reviews*, *160*, 3–23. https://doi.org/10.1007/s11214-010-9740-1

Hietala, H., Laitinen, T. V., Andréeová, K., Vainio, R., Vaivads, A., Palmroth, M., … Rème, H. (2009). Supermagnetosonic jets behind a collisionless quasiparallel shock. *Physical Review Letters*, *103*, 245001. https://doi.org/10.1103/PhysRevLett.103.245001

Hietala, H., & Plaschke, F. (2013). On the generation of magnetosheath high-speed jets by bow shock ripples. *Journal of Geophysical Research: Space Physics*, *118*, 7237–7245. https://doi.org/10.1002/2013JA019172

Huang, S. Y., Retinò, A., Phan, T. D., Daughton, W., Vaivads, A., Karimabadi, H., … Wang, D. D. (2016). In situ observations of flux rope at the separatrix region of magnetic reconnection. *Journal of Geophysical Research: Space Physics*, *121*, 205–213. https://doi.org/10.1002/2015JA021468

Huang, S. Y., Sahraoui, F., Yuan, Z. G., He, J. S., Zhao, J. S., Le Contel, O., … Burch, J. L. (2017). Magnetospheric Multiscale observations of electron vortex magnetic hole in the turbulent magnetosheath plasma. *The Astrophysical Journal Letters*, *836*(2), L27. https://doi.org/10.3847/2041-8213/aa5f50

Karimabadi, H., Roytershteyn, V., Vu, H. X., Omelchenko, Y. A., Scudder, J., Daughton, W., … Geveci, B. (2014). The link between shocks, turbulence, and magnetic reconnection in collisionless plasmas. *Physics of Plasmas*, *21*, 62308. https://doi.org/10.1063/1.4882875

Khrabrov, A. V., & Sonnerup, B. U. Ö. (1998). DedeHoffmann-teller analysis. In G. Paschmann & P. W. Daly (Eds.), *Multi-spacecraft analysis methods, ISSI Scientific Reports Series SR-001* (pp. 221–248). Noordwijk, Netherlands: ESA Communication.

Knetter, T., Neubauer, F. M., Horbury, T., & Balogh, A. (2004). Four-point discontinuity observations using Cluster magnetic field data: A statistical survey. *Journal of Geophysical Research*, *109*, A06102. https://doi.org/10.1029/2003JA010099

Lavraud, B., Ruffenach, A., Rouillard, A. P., Kajdic, P., Manchester, W. B., & Lugaz, N. (2014). Geo-effectiveness and radial dependence of magnetic cloud erosion by magnetic reconnection. *Journal of Geophysical Research: Space Physics*, *119*, 26–35. https://doi.org/10.1002/2013JA019154

Le, A., Egedal, J., Ohia, O., Daughton, W., Karimabdai, H., & Lukin, V. S. (2013). Regimes of the electron diffusion region in magnetic reconnection. *Physical Review Letters*, *110*, 135004. https://doi.org/10.1103/PhysRevLett.110.135004

Le Contel, O., Leroy, P., Roux, A., Coillot, C., Alison, D., Bouabdellah, A., … de la Porte, B. (2016). The search-coil magnetometer for MMS. *Space Science Reviews*, *199*, 257–282. https://doi.org/10.1007/s11214-014-0096-9

Lindqvist, P. A., Olsson, G., Torbert, R. B., King, B., Granoff, M., Rau, D., … Tucker, S. (2016). The spin-plane double probe electric field instrument for MMS. *Space Science Reviews*, *199*, 137–165. https://doi.org/10.1007/s11214-014-0116-9

Matthaeus, W. H., & Lamkin, S. L. (1986). Turbulent magnetic reconnection. *Physics of Fluids*, *29*(8), 2513–2534.

McComas, D. J., Gosling, J. T., Hammond, C. M., Moldwin, M. B., Phillips, J. L., & Forsyth, R. J. (1994). Magnetic reconnection ahead of a coronal mass ejection. *Geophysical Research Letters*, *21*, 1751–1754. https://doi.org/10.1029/94GL01077

Nagai, T., Shinohara, I., Fujimoto, M., Matsuoka, A., Saito, Y., & Mukai, T. (2011). Construction of magnetic reconnection in the near-Eearth magnetotail with Geotail. *Journal of Geophysical Research*, *116*, A04222. https://doi.org/10.1029/2010JA016283

Nagai, T., Shinohara, I., & Zenitani, S. (2015). Ion acceleration processes in magnetic reconnection: Geotail observations in the magnetotail. *Journal of Geophysical Research: Space Physics*, *120*, 1766–1783. https://doi.org/10.1002/2014JA020737

Nakamura, R., Baumjohann, W., Asano, Y., Runov, A., Balogh, A., Owen, C. J., … Rème, H. (2006). Dynamics of thin current sheets associated with magnetotail reconnection. *Journal of Geophysical Research*, *111*, A11206. https://doi.org/10.1029/2006JA011706

Norgren, C., Graham, D. B., Khotyainstev, Y. V., André, M., Vaivads, A., Chen, L. J., … Burch, J. L. (2016). Finite gyroradius effects in the electron outflow of asymmetric magnetic reconnection. *Geophysical Research Letters*, *43*, 6724–6733. https://doi.org/10.1002/2016GL069205

Øieroset, M., Phan, T. D., Fujimoto, M., Lin, R. P., & Lepping, R. P. (2001). In situ detection of collisionless reconnection in the Earth's magnetotail. *Nature*, *412*, 414–417. https://doi.org/10.1038/35086520

Øieroset, M., Phan, T. D., Lin, R. P., & Sonnerup, B. U. Ö. (2000). Walén and variance analysis of high-speed flows observed by Wind in the midtail plasma sheet: Evidence for reconnection. *Journal of Geophysical Research*, *105*(A11), 25,247–25,263.

Osman, K. T., Matthaeus, W. H., Greco, A., & Servidio, S. (2011). Evidence for inhomogeneous heating in the solar wind. *Astrophysics Journal*, *727*, L11. https://doi.org/10.1088/2041-8205/727/1/L11

Osman, K. T., Wan, M., Matthaeus, W. H., Breech, B., & Oughton, S. (2011). Directional alignment and non-Gaussian statistics in solar wind turbulence. *Astrophysics Journal*, *741*, 75. https://doi.org/10.1088/0004-637X/741/2/75

Paschmann, G., Haaland, S., Sonnerup, B. U. Ö., Hasegawa, H., Georgescu, E., Klecker, B., … Vaivads, A. (2005). Characteristics of the near-tail dawn magnetopause and boundary layer. *Annales Geophysicae*, *23*, 1481–1497.

Paschmann, G., & Sonnerup, B. U. Ö. (2008). Proper frame determination and Walen test. In *Multi-spacecraft analysis methods revisited, ISSI Scientific Reports Series SR-008* (pp. 65–74). Noordwijk, Netherlands: ESA Communication.

Paschmann, G., Sonnerup, B. U. Ö., Papamastorakis, I., Sckopke, N., Haerendel, G., Bame, S. J., … Elphic, R. C. (1979). Plasma acceleration at the Earth's magnetopause: Evidence for reconnection. *Nature*, *282*, 243–246. https://doi.org/10.1038/282243a0

Phan, T. D., Drake, J. F., Shay, M. A., Mozer, F. S., & Eastwood, J. P. (2007). Evidence for an elongated (>60 ion skin depth electron diffusion region during fast magnetic reconnection. *Physical Review Letters*, *99*, 255002. https://doi.org/10.1103/PhysRevLett.99.255002

Phan, T. D., Dunlop, M. W., Paschmann, G., Klecker, B., Bosqued, J. M., Rème, H., … Kistler, L. M. (2004). Cluster observations of continuous reconnection at the magnetopause under steady interplanetary magnetic field conditions. *Annales de Geophysique*, *22*, 2355–2367.

Phan, T. D., Gosling, J. T., Paschmann, G., Pasma, C., Drake, J. F., Øieroset, M., … Davis, M. S. (2010). The dependence of magnetic reconnection on plasma β and magnetic shear: Evidence from solar wind observations. *The Astrophysical Journal Letters*, *719*, L199–L203. https://doi.org/10.1088/2041-8205/719/2/L199

Phan, T. D., Paschmann, G., Twitty, C., Mozer, F. S., Gosling, J. T., Eastwood, J. P., … Lucek, E. A. (2007). Evidence for magnetic reconnection initiated in the magnetosheath. *Geophysical Research Letters*, *34*, L14104. https://doi.org/10.1029/2007GL030343

Plaschke, F., Hietala, H., Angelopoulos, V., & Nakamura, R. (2016). Geoeffective jets impacting the magnetopause are very common. *Journal of Geophysical Research: Space Physics*, *121*, 3240–3253. https://doi.org/10.1002/2016JA022534

Pollock, C., Moore, T., Jacques, A., Burch, J., Gliese, U., Saito, Y., … Zeuch, M. (2016). Fast plasma investigation for magnetospheric multiscale. *Space Science Reviews*, *199*, 331–406. https://doi.org/10.1007/s11214-016-0245-4

Retinò, A., Sundkvist, D., Vaivads, A., Mozer, F., André, M., & Owen, C. J. (2007). In situ evidence of magnetic reconnection in turbulent plasma. *Nature Physics*, *3*, 236–238. https://doi.org/10.1038/nphys574

Ruffenach, A., Lavraud, B., Farrugia, C. J., DÃl'moulin, P., Dasso, S., Owens, M. J., … Galvin, A. B. (2015). Statistical study of magnetic cloud erosion by magnetic reconnection. *Journal of Geophysical Research: Space Physics*, *120*, 43–60. https://doi.org/10.1002/2014JA020628

Runov, A., Nakamura, R., Baumjohann, W., Treumann, R. A., Zhang, T. L., Volwerk, M., … Kistler, L. (2003). Current sheet structure near magnetic X-line observed by Cluster. *Geophysical Research Letters*, *30*(11), 1579. https://doi.org/10.1029/2002GL016730

Russell, C. T., Anderson, B. J., Baumjohann, W., Bromund, K. R., Dearborn, D., Fischer, D., … Richter, I. (2016). The magnetospheric multiscale magnetometers. *Space Science Reviews*, *199*, 189–256. https://doi.org/10.1007/s11214-014-0057-3

Russell, C. T., & Elphic, R. C. (1979). ISEE observations of flux transfer events at the dayside magnetopause. *Geophysical Research Letters*, *6*(1), 33–36. https://doi.org/10.1029/GL006i001p00033

Samsonov, A. A., Pudovkin, M. I., Gary, S. P., & Hubert, D. (2001). Anisotropic MHD model of the dayside magnetosheath downstream of the oblique bow shock. *Journal of Geophysical Research*, *106*(A10), 21,689–21,699.

Savin, S., Amata, E., Zelenyi, L., Nemecek, Z., Borodkova, N., Buechner, J., … Lezhen, L. (2012). Super fast plasma streams as drivers of transient and anomalous magnetospheric dynamics. *Annales de Geophysique*, *30*, 1–7. https://doi.org/10.5194/angeo-30-1-2012

Scudder, J., & Daughton, W. (2008). "Illuminating" electron diffusion regions of collisionless magnetic reconnection using electron agyrotropy. *Journal of Geophysical Research*, *113*, A06222. https://doi.org/10.1029/2008JA013035

Scholer, M, Thomsen, M. F., Burgess, D., Bale, S. D., Balikhin, M., Balogh, A., … Walker, S. N. (2005). Cluster at the bow shock. *Space Science Reviews*, *118*, 155–160. https://doi.org/10.1007/s11214-005-3826-1

Servidio, S., Greco, A., Matthaeus, W. H., Osman, K. T., & Dmitruk, P. (2011). Statistical association of discontinuities and reconnection in magnetohydrodynamic turbulence. *Journal of Geophysical Research*, *116*, A09102. https://doi.org/10.1029/2011JA016569

Shay, M. A., Drake, J. F., & Swisdak, M. (2007). Two-scale structure of the electron dissipation region during collisionless magnetic reconnection. *Physical Review Letters*, *99*, 155002. https://doi.org/10.1103/PhysRevLett.99.155002

Shay, M. A., Phan, T. D., Haggerty, C. C., Fujimoto, M., Drake, J. F., Malakit, K., … Swisdak, M. (2016). Kinetic signatures of the region surrounding the X line in asymmetric (magnetopause) reconnection. *Geophysical Research Letters*, *43*, 4145–4154. https://doi.org/10.1002/2016GL069034

Sibeck, D. G., Kudela, K., Lepping, R. P., Lin, R., Nemecek, Z., Nozdrachev, M. N., … Yermolaev, Y. (2000). Magnetopause motion driven by interplanetary magnetic field variations. *Journal of Geophysical Research*, *105*, 25,155–25,170. https://doi.org/10.1029/2000JA900109

Sonnerup, B. U. Ö., Haaland, S. E., & Paschmann, G. (2008). Discontinuity orientation, motion, and thickness. In *Multi-Spacecraft Analysis Methods Revisited, ISSI Scientific Reports Series SR-008* (pp. 1–15). Noordwijk, Netherlands: ESA Communication.

Sonnerup, B. U. Ö., Papamastorakis, I., Paschmann, G., & Luehr, H. (1987). Magnetopause properties from AMPTE/IRM observations of the convection electric field. Method development. *Journal of Geophysical Research*, *92*, 12,137–12,159.

Sonnerup, B. U. Ö., & Scheible, M. (1998). Minimum and maximum variance analysis. In G. Paschmann & P. W. Daly (Eds.), *Analysis methods for multi-spacecraft data, ISSI Scientific Reports Series SR-001* (pp. 185–220). Noordwijk, Netherlands: ESA Communication.

Sundqvist, D., Retinò, A., Vaivads, A., & Bale, S. D. (2007). Dissipation in turbulent plasma due to reconnectionin thin current sheets. *Physical Review Letters*, *99*, 25004. https://doi.org/10.1103/PhysRevLett.99.025004

Swisdak, M. (2016). Quantifying gyrotropy in magnetic reconnection. *Geophysical Research Letters*, *43*, 43–49. https://doi.org/10.1002/2015GL066980

Torbert, R. B., Russell, C. T., Magnes, W., Ergun, R. E., Lindqvist, P.-A., LeContel, O., … Lappalainen, K. (2016). The FIELDS instrument suite on MMS: Scientific objectives, measurements, and data products. *Space Science Reviews*, *199*, 105–135. https://doi.org/10.1007/s11214-014-0109-8

Vörös, Z., Facskó, G., Khodachenko, M., Honkonen, I., Janhunen, P., & Palmroth, M. (2014). Windsock memory COnditioned RAM (CO-RAM) pressure effect: Forced reconnection in the Earth's magnetotail. *Journal of Geophysical Research*, *119*, 6273–6293. https://doi.org/10.1002/2014JA019857

Vörös, Z., Yordanova, E., Echim, M. M., Consolini, G., & Narita, Y. (2016). Turbulence-generated proton-scale structures in the terrestrial magnetosheath. *The Astrophysical Journal Letters*, *819*, L15. https://doi.org/10.3847/2041-8205/819/1/L15

Wan, M., Matthaeus, W. H., Roytershteyn, V., Karimabadi, H., Parashar, T., Wu, P., & Shay, M. (2015). Intermittent dissipation and heating in 3D kinetic plasma turbulence. *Physical Review Letters*, *114*, 175002. https://doi.org/10.1103/PhysRevLett.114.175002

Yordanova, E., Vaivads, A., André, M., Buchert, S. C., & Vörös, Z. (2008). Magnetosheath plasma turbulence and its spatiotemporal evolution as observed by the Cluster spacecraft. *Physical Review Letters*, *100*, 205003. https://doi.org/10.1103/PhysRevLett.100.205003

Yordanova, E., Vörös, Z., Varsani, A., Graham, D. B., Norgren, C., Khotyainstev, Y. V., … Saito, Y. (2016). Electron scale structures and magnetic reconnection signatures in the turbulent magnetosheath. *Geophysical Research Letters*, *43*, 5969–5978. https://doi.org/10.1002/2016GL069191

Zenitani, S., & Nagai, T. (2016). Particle dynamics in the electron current layer in collisionless magnetic reconnection. *Physics of Plasmas*, *23*, 102102. https://doi.org/10.1063/1.4963008

Zhang, Y. C. (2016). Distinct characteristics of asymmetric magnetic reconnections: Observational results from the exhaust region at the dayside magnetopause. *Nature Scientific Reports*, *6*, 27592. https://doi.org/10.1038/srep27592

Zhou, X.-Z., Angelopoulos, V., Runov, A., Sitnov, M. I., Zong, Q.-G., & Pu, Z. Y. (2009). Ion distributions near the reconnection sites: Comparison between simulations and THEMIS observations. *Journal of Geophysical Research*, *114*, A12211. https://doi.org/10.1029/2009JA014614

Zhou, M., Deng, X., Tang, R., Pang, Y., Xu, X., Yuan, Z., & Huang, S. (2014). Evidence of deflected super-Alfvénic electron jet in a reconnection region with weak guide field. *Journal of Geophysical Research: Space Physics*, *119*, 1541 – 1548. https://doi.org/10.1002/2013JA019556